On machine learning assisted data-driven bridging of FSDT and HOZT for high-fidelity uncertainty quantification of laminated composite and sandwich plates

Vaishali[a], T. Mukhopadhyay[b,*], S. Naskar[c], S. Dey[a]

[a]*Department of Mechanical Engineering, National Institute of Technology Silchar, Assam, India*

[b]*Department of Aerospace Engineering, Indian Institute of Technology Kanpur, Kanpur, India*

[c]*Faculty of Engineering and Physical Sciences, University of Southampton, Southampton, UK*

**Email address: tanmoy@iitk.ac.in*

Abstract

First-order shear deformation theory (FSDT) is less accurate compared to higher-order theories like higher-order zigzag theory (HOZT).In case of large-scale simulation-based analyses like uncertainty quantification and optimization using FSDT, such errors propagate and accumulate over multiple realizations, leading to significantly erroneous results. Consideration of higher-order theories results in significantly increased computational expenses, even though these theories are more accurate. The aspect of computational efficiency becomes more critical when thousands of realizations are necessary for the analyses. Here we propose to exploit Gaussian process-based machine learning for creating a computational bridging between FSDT and HOZT, wherein the accuracy of HOZT can be achieved while having the low computational expenses of FSDT. The machine learning augmented FSDT algorithm is referred to here as modified FSDT (mFSDT), based on which extensive deterministic results and Monte Carlo simulation-assisted probabilistic results are presented for the free vibration analysis of shear deformation sensitive structures like laminated composite and sandwich plates considering various configurations. The proposed algorithm of bridging different laminate theories is generic in nature and it can be utilized further in a range of other static and dynamic analyses concerning composite plates and shells for accurate, yet efficient results.

Keywords: Modified first-order shear deformation theory (mFSDT); Higher order zigzag theory (HOZT); Gaussian process regression; Monte Carlo simulation; Data-driven stochastic natural frequency analysis; Machine learning assisted laminate theory

1. Introduction

Many of the lightweight structures in aerospace, mechanical, naval and civil engineering applications are made up of laminated composites and sandwich configurations because of their advantageous properties like high strength and stiffness to weight ratio, thermal properties and a range of other multi-physical aspects. These structures also allow bespoke optimization in mechanical components design by providing the option of tailoring material distribution with varying properties according to the loading paths. In laminated composites, the structures are formed by heaping piles made of composite materials with particular fiber orientations in each layer. In contrast, for sandwich structures, there is a core, which is of lightweight fabric, placed between two thin but stiff faces. The faces can be made of composite laminates or a monolithic material layer. A sandwich configuration with laminated face sheets (refer to figure 1) provides the dual advantage of weight reduction with high bending stiffness and application-specific tailoring of directional material properties based on fiber orientation in each layer.

Consideration of accurate shear deformation is crucial in the sandwich structures with laminated composite face sheets (i.e. laminated composites and sandwich plates) for obtaining reliable results. The complicated construction and manufacturing process of these structures causes high random variation in the material and geometric properties [66 - 72], resulting in an uncertain behavior along with complex distribution of shear. Moreover, these structures often need to accommodate skewness in the geometry, adding the possibility of accumulating further undesirable uncertainties. So, it becomes extremely challenging to determine the vibration responses of such laminated composite sandwich plates precisely in the existence of inherent random fluctuations in the material and geometric properties for different specified thicknesses and degrees of orthotropy. Therefore, the present study is focused on stochastic natural frequency analysis of laminated composite and sandwich structures including the effect of such material and geometric specifications.

The backbone of effective stochastic analysis and uncertainty quantification is an accurate, yet efficient deterministic theory. Various plate theories have been developed for the deterministic analysis of laminated composite and sandwich structures, which are broadly classified into two

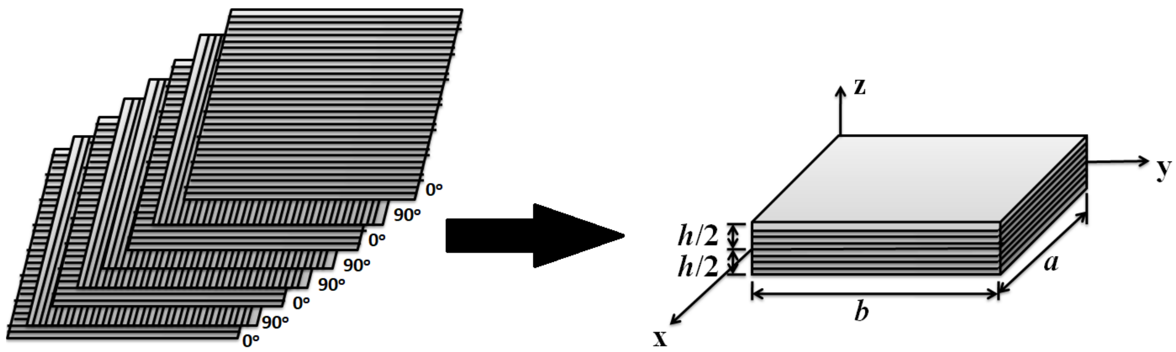

(a)

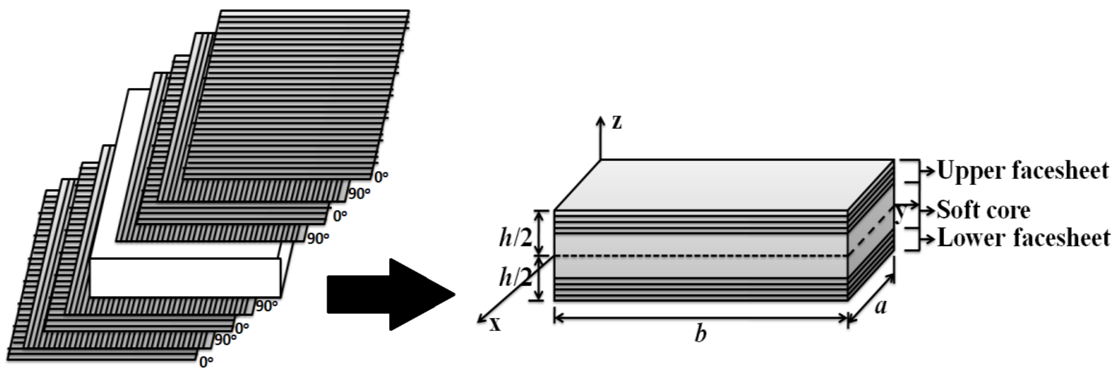

(b)

Fig. 1: (a) A typical example of eight layered laminated composite structure (0°/90°/0°/90°)s (b) A sandwich structure with (0°/90°/0°/90°/core/90°/0°/90°/0°) ply configuration (referred here as laminated composite and sandwich structure).

types: single layer theory (SLT) and layer-wise theory (LWT). In single layer theory, the deformation of plate is expressed in terms of unknown parameters of the reference plane, i.e. middle plane. In this theory, the transverse shear strain is assumed to be uniform over the entire plate thickness and it is known as Reissner-Mindlin's plate theory [47]. Different classical theories came into the picture for studying the bending, buckling, vibration, etc., of composite structures like the classical plate theory (CPT), first-order deformation theory (FSDT), and higher-order shear deformation theory (HSDT). In CPT, the transverse shear effect is neglected; therefore, this theory provides reasonable results in thin plates, but it does not give satisfactory results for the thick plate. To overcome this problem, FSDT and HSDT were developed. FSDT is based on Resissner [1] and Mindlin [2], where the displacement is linearly modelled throughout the thickness. According to FSDT, the transverse shear strain is approximated by incorporating a shear correction factor through the thickness which is also unable to predict the actual behaviour of composite laminates [52]. A large number of studies have been carried out for the case of free vibration analysis of composite plates [3-15] focusing on deterministic aspects. To overcome the limitations of FSDT, later HSDT was developed. The HSDT was developed by several researchers [16-21] to obtain more accurate solution by eliminating the discrepancies between actual and assumed distribution of shear deformation through the thickness of laminate [52]. This theory involves the non-linear vibration of displacement field through the thickness using Taylor's series up to 3rd order. Later, LWT was developed, which uses a continuous displacement field through each layer of a laminate [47]. This theory is further classified into discrete layer-plate theory (DLT) and refined plate theory (RPT). In DLT, unknown components are taken at all the layer interfaces [22-27]. It was found that this theory provides satisfactory results, wherein for fewer layers, it can easily be applied. As we increase the number of layers, a large number of unknowns related to the number of layers, make the complete process computationally exhaustive. This problem was solved by developing a new theory known as RPT, where the unknowns at the different interfaces were defined in terms of that of the reference plane. Here, it was considered to have a piecewise variation of displacement throughout the thickness. Therefore the number of unknowns was not dependent on the number of layers. Based on Carrera Unified Formulation (CUF), Carrera [53] has introduced a unified 1D finite element for the analysis of soft material structures. CUF has been extended to deal with linear elastic geometrical nonlinear analyses of beams [54], plates [55] and shells [56]. The results have shown great capabilities for FE to deal with static large displacement analysis, dynamics [57], and analysis of laminated structures, eventually providing accurate inter-laminar stress fields [88]. Many researchers like Carrera [28], Chakrabarti and Sheikh [29], Akhras and Li [30], Kulkarni and Kapuria [31], and others [32-35] have utilized HOZT in their analysis. It was observed that this theory provides very accurate results. However, the main problem with it is in its finite element (FE) implementation as it needs C_1 continuity of the transverse displacement of nodes. Moreover, the accuracy comes here at an expense of additional computational burden, which is a crucial factor in a range of analyses where thousands of simulations are necessary. In this context, many researchers [39, 40, 46, 48, 49, 59 - 66] have integrated surrogate models (/machine learning) with FE to increase computational efficiency.

In general, first-order shear deformation theory (FSDT) is less accurate compared to higher-order theories like higher-order zigzag theory (HOZT). In case of large-scale simulation-based analyses like uncertainty quantification and optimization using FSDT, such errors propagate and accumulate over multiple realizations, leading to significantly erroneous results. Consideration of higher-order theories results in significantly increased computational expenses, even though these theories are more accurate. The aspect of computational efficiency becomes more critical when thousands of realizations are necessary for the analyses. In this paper, we aim to exploit Gaussian process-based machine learning for creating a computational bridging between FSDT and HOZT, wherein the accuracy of HOZT can be achieved while having the low computational expenses of FSDT. Based on the machine learning augmented FSDT algorithm (i.e. the modified FSDT, or mFSDT), extensive deterministic results and Monte Carlo simulation-assisted probabilistic results would be presented here for the stochastic free vibration analysis of shear deformation sensitive structures like laminated composite and sandwich plates. We aim to investigate both sandwich structures with laminated face sheets (referred to as laminated composite and sandwich structures) as well as conventional composite laminates (note that conventional composite laminates can essentially be thought as a special case of the laminated composite and sandwich structures as presented in figure 1). The novelty of the present study lies in its machine learning based model building, where we augment the accuracy of FSDT to the level of HOZT by bridging their difference through the GPR based mapping, while keeping the computational expenses similar to that of the original FSDT. The proposed algorithm of bridging different laminate theories is generic in nature and it can be utilized further for connecting other deformation theories to develop a unified framework, leading to a range of large-scale data-driven static and dynamic analyses of complex structural forms for accurate, yet computationally efficient predictions.

Hereafter, the present paper is divided into multiple sections; section 2 deals with the mathematical formulation for free vibration using HOZT theory and FSDT theory along with the

Gaussian process-based machine learning algorithm for mFSDT; section 3 contains results and discussion covering deterministic and stochastic simulations, and section 4 provides the concluding remark and future outlook.

2. Mathematical formulation

In this section, we systematically provide the mathematical formulation of different components involved in the proposed approach for stochastic free vibration analysis. In the first two subsections, the fundamental concepts of higher order zigzag theory (HOZT) and first order shear deformation theory (FSDT) are presented, followed by the free vibration analysis based on these two theories and their finite element implementation. Subsequently, the mathematical background of Gaussian Process based machine learning is briefly discussed. We then propose the concept of modified first-order shear deformation theory (mFSDT), based on which an efficient framework of stochastic free vibration analysis is developed thereafter.

2.1. Higher order zigzag theory (HOZT)

We consider a general laminate configuration of stochastic skew angle $\phi(\tilde{\omega})$ having '*n*' number of the thin lamina. The symbol '$\tilde{\omega}$' represents the degree of stochasticity in the respective input parameters. Let us consider 'θ' as the fiber orientation angle with respect to structural axis system '(*x*-*y*-*z*)'. The normal stress vector is indicated by $\{\sigma(\tilde{\omega})\}$, the shear stress is indicated by $\{\tau(\tilde{\omega})\}$, while the normal strain vector is represented by $\{\varepsilon(\tilde{\omega})\}$, and the shear strain vector is represented by $\{\gamma(\tilde{\omega})\}$. $[Q_k(\tilde{\omega})]$ represents the transformed rigidity matrix of *k*-th lamina. Hence, the stress-strain relationship [36] can be written as

$\{\sigma(\tilde{\omega})\} = [Q_k(\tilde{\omega})]\{\varepsilon(\tilde{\omega})\}$, i. e.

$$\begin{Bmatrix} \sigma_{xx}(\tilde{\omega}) \\ \sigma_{yy}(\tilde{\omega}) \\ \sigma_{zz}(\tilde{\omega}) \\ \tau_{xy}(\tilde{\omega}) \\ \tau_{xz}(\tilde{\omega}) \\ \tau_{yz}(\tilde{\omega}) \end{Bmatrix} = \begin{bmatrix} Q_{11}(\tilde{\omega}) & Q_{12}(\tilde{\omega}) & Q_{13}(\tilde{\omega}) & Q_{14}(\tilde{\omega}) & 0 & 0 \\ Q_{21}(\tilde{\omega}) & Q_{22}(\tilde{\omega}) & Q_{23}(\tilde{\omega}) & Q_{24}(\tilde{\omega}) & 0 & 0 \\ Q_{31}(\tilde{\omega}) & Q_{32}(\tilde{\omega}) & Q_{33}(\tilde{\omega}) & Q_{34}(\tilde{\omega}) & 0 & 0 \\ Q_{41}(\tilde{\omega}) & Q_{42}(\tilde{\omega}) & Q_{43}(\tilde{\omega}) & Q_{44}(\tilde{\omega}) & 0 & 0 \\ 0 & 0 & 0 & 0 & Q_{55}(\tilde{\omega}) & Q_{56}(\tilde{\omega}) \\ 0 & 0 & 0 & 0 & Q_{65}(\tilde{\omega}) & Q_{66}(\tilde{\omega}) \end{bmatrix}_k \begin{Bmatrix} \varepsilon_{xx}(\tilde{\omega}) \\ \varepsilon_{yy}(\tilde{\omega}) \\ \varepsilon_{zz}(\tilde{\omega}) \\ \gamma_{xy}(\tilde{\omega}) \\ \gamma_{xz}(\tilde{\omega}) \\ \gamma_{yz}(\tilde{\omega}) \end{Bmatrix} \tag{1}$$

The mid-plane of the plate is considered as the reference plane for in-plane displacement field ($u\left(\tilde{\omega}\right), v\left(\tilde{\omega}\right)$) calculation, which can be expressed as

$$u\left(\tilde{\omega}\right) = u_0(\tilde{\omega}) + z\theta_x(\tilde{\omega}) + \sum_{i=1}^{n_u-1}\left(z - z_i^u\right)\left(\tilde{\omega}\right)H\left(z - z_i^u\right)\beta_{xu}^i + \sum_{j=1}^{n_l-1}\left(z - z_j^l\right)\left(\tilde{\omega}\right)H\left(-z + z_j^l\right)\beta_{xl}^j + \alpha_x z^2 + \psi_x z^3 \tag{2}$$

$$v\left(\tilde{\omega}\right) = v_0(\tilde{\omega}) + z\theta_y(\tilde{\omega}) + \sum_{i=1}^{n_u-1}\left(z - z_i^u\right)\left(\tilde{\omega}\right)H\left(z - z_i^u\right)\beta_{yu}^i + \sum_{j=1}^{n_l-1}\left(z - z_j^l\right)\left(\tilde{\omega}\right)H\left(-z + z_j^l\right)\beta_{yl}^j + \alpha_y z^2 + \psi_y z^3 \tag{3}$$

Here $(\theta_x(\tilde{\omega}),\ \theta_y(\tilde{\omega}))$ and $(u_0(\tilde{\omega}),\ v_0(\tilde{\omega}))$ are the rotation and displacements of the mid-plane along the x and y-axis, respectively. The number of the upper and lower layers is denoted as $(n_u,\ n_l, n = n_u + n_l)$ respectively, while $(\alpha_x,\ \alpha_y,\ \psi_x, \psi_y)$ are the higher-order unknown co-efficient and $(\beta_{xu}^i,\ \beta_{yu}^j, \beta_{xl}^i,\ \beta_{yl}^j)$ are the slope of i^{th} and j^{th} layer corresponding to the upper and lower layer, respectively. $H\left(z - z_i^u\right)$ and $H\left(-z + z_j^l\right)$ are unit step functions. For transverse displacement, variation throughout is given as

$$w\left(\tilde{\omega}\right) = \frac{z(z + t_l)}{t_u(t_u + t_l)} w_u\left(\tilde{\omega}\right) + \frac{(z + t_l)(t_u - z)}{t_l t_u} w_0\left(\tilde{\omega}\right) + \frac{z(t_u - z)}{-t_l(t_u + t_l)} w_l\left(\tilde{\omega}\right) \tag{4}$$

$$\text{For upper face layers,} \quad w\left(\tilde{\omega}\right) = w_u\left(\tilde{\omega}\right) \tag{5}$$

$$\text{For lower face layers,} \quad w\left(\tilde{\omega}\right) = w_l\left(\tilde{\omega}\right) \tag{6}$$

The transverse displacement values at the lower layer are denoted as $w_l(\tilde{\omega})$, at upper layer denoted as $w_u(\tilde{\omega})$, whereas $w_o(\tilde{\omega})$ represents that for the middle layer. Zero transverse shear stress condition is considered at top and bottom surfaces. At interfaces, applying the conditions of the transverse shear stress continuity between the layers, at top layer: $\dot{u}(\tilde{\omega}) = u_u(\tilde{\omega})$, $\dot{v}(\tilde{\omega}) = v_u(\tilde{\omega})$ and at bottom layer: $\dot{u}(\tilde{\omega}) = u_l(\tilde{\omega})$, $\dot{v}(\tilde{\omega}) = v_l(\tilde{\omega})$. Here α_x, α_y, ψ_x, ψ_y, β_{xu}^i, β_{yu}^j, β_{xl}^i, β_{yl}^j, $(\partial w_u(\tilde{\omega})/\partial x)$, $(\partial w_l(\tilde{\omega})/\partial x)(\partial w_u(\tilde{\omega})/\partial y)$, $(\partial w_l(\tilde{\omega})/\partial y)$ can be expressed in displacement terms $(u_0(\tilde{\omega}),\ v_0(\tilde{\omega}), \theta_x(\tilde{\omega}), \theta_y(\tilde{\omega}), u_u(\tilde{\omega}), u_l(\tilde{\omega}), v_u(\tilde{\omega}), v_l(\tilde{\omega}))$ as

$$\left\{\tilde{B}(\tilde{\omega})\right\} = \left[\tilde{A}(\tilde{\omega})\right]\left\{\beta(\tilde{\omega})\right\},$$

where

$$\left\{\tilde{B}(\tilde{\omega})\right\} = \begin{Bmatrix} \alpha_x\psi_x\alpha_y\psi_y\beta_{xu}^1\beta_{xu}^2\ldots\beta_{xu}^{nu-1}\beta_{xl}^1\beta_{xl}^2\ldots\beta_{xl}^{nl-1}\beta_{yu}^1\beta_{yu}^2\ldots\beta_{yu}^{nu-1}\beta_{yl}^1\beta_{yl}^2\ldots\beta_{yl}^{nl-1} \\ \left(\partial w_u(\tilde{\omega})/\partial x\right)\left(\partial w_u(\tilde{\omega})/\partial y\right)\left(\partial w_1(\tilde{\omega})/\partial x\right)\left(\partial w_1(\tilde{\omega})/\partial y\right) \end{Bmatrix}^T, \tag{7}$$

$$\left\{\beta(\tilde{\omega})\right\} = \left\{u_0(\tilde{\omega})v_0(\tilde{\omega})\theta_x(\tilde{\omega})\theta_y(\tilde{\omega})u_u(\tilde{\omega})v_u(\tilde{\omega})u_l(\tilde{\omega})v_l(\tilde{\omega})\right\}^T$$

The elements of $\left[\tilde{A}(\tilde{\omega})\right]$ are dependent on material properties. Using the above equations, the in-plane displacement fields can be expressed as

$$\begin{aligned} u(\tilde{\omega}) &= b_1u_0(\tilde{\omega}) + b_2v_0(\tilde{\omega}) + b_3\theta_x(\tilde{\omega}) + b_4\theta_y(\tilde{\omega}) + b_5u_u(\tilde{\omega}) + b_6v_u(\tilde{\omega}) + b_7u_1(\tilde{\omega}) + b_8v_l(\tilde{\omega}), \\ v(\tilde{\omega}) &= c_1u_0(\tilde{\omega}) + c_2v_0(\tilde{\omega}) + c_3\theta_x(\tilde{\omega}) + c_4\theta_y(\tilde{\omega}) + c_5u_u(\tilde{\omega}) + c_6v_u(\tilde{\omega}) + c_7u_l(\tilde{\omega}) + c_8v_l(\tilde{\omega}), \end{aligned} \tag{8}$$

where, the coefficients of b_i's and c_i's are function of thickness coordinates, unit step functions and material properties. For details, one can refer to [36] . The generalized displacement vector $\left\{\delta(\tilde{\omega})\right\}$ can be given as

$$\left\{\delta(\tilde{\omega})\right\} = \left\{u_0(\tilde{\omega})\ \ v_0(\tilde{\omega})\ \ w_0(\tilde{\omega})\ \ \theta_x(\tilde{\omega})\ \ \theta_y(\tilde{\omega})\ \ u_u(\tilde{\omega})\ \ v_u(\tilde{\omega})\ \ w_u(\tilde{\omega})\ \ u_l(\tilde{\omega})\ \ v_l(\tilde{\omega})\ \ w_l(\tilde{\omega})\right\}^T \tag{9}$$

Utilizing linear strain-displacement relation and eqs. (1-7), the strain field can be expressed as:

$$\left\{\hat{\varepsilon}(\tilde{\omega})\right\} = \left[\frac{\partial u(\tilde{\omega})}{\partial x}\ \ \frac{\partial v(\tilde{\omega})}{\partial y}\ \ \frac{\partial w(\tilde{\omega})}{\partial z}\ \ \frac{\partial u(\tilde{\omega})}{\partial y} + \frac{\partial v(\tilde{\omega})}{\partial x}\ \ \frac{\partial u(\tilde{\omega})}{\partial z} + \frac{\partial w(\tilde{\omega})}{\partial x}\ \ \frac{\partial v(\tilde{\omega})}{\partial z} + \frac{\partial w(\tilde{\omega})}{\partial y}\right]$$

i.e. $\left\{\hat{\varepsilon}(\tilde{\omega})\right\} = \left[H(\tilde{\omega})\right]\left\{\varepsilon(\tilde{\omega})\right\}$,

where,

$$\begin{aligned} \left\{\varepsilon(\tilde{\omega})\right\} = [&u_0(\tilde{\omega})\ v_0(\tilde{\omega})\ w_0(\tilde{\omega})\ \theta_x(\tilde{\omega})\ \theta_y(\tilde{\omega})\ u_u(\tilde{\omega})\ v_u(\tilde{\omega})\ w_u(\tilde{\omega})\ u_l(\tilde{\omega})\ v_l(\tilde{\omega})\ w_l(\tilde{\omega}) \\ &\left(\partial u_0(\tilde{\omega})/\partial x\right)\ \left(\partial u_0(\tilde{\omega})/\partial y\right)\ \left(\partial v_0(\tilde{\omega})/\partial x\right)\ \left(\partial v_0(\tilde{\omega})/\partial y\right)\ \left(\partial w_0(\tilde{\omega})/\partial x\right)\ \left(\partial w_0(\tilde{\omega})/\partial y\right) \\ &\left(\partial\theta_x(\tilde{\omega})/\partial x\right)\ \left(\partial\theta_x(\tilde{\omega})/\partial y\right)\ \left(\partial\theta_y(\tilde{\omega})/\partial x\right)\ \left(\partial\theta_y(\tilde{\omega})/\partial y\right)\ \left(\partial u_u(\tilde{\omega})/\partial x\right)\ \left(\partial u_u(\tilde{\omega})/\partial y\right) \\ &\left(\partial v_u(\tilde{\omega})/\partial x\right)\ \left(\partial v_u(\tilde{\omega})/\partial y\right)\ \left(\partial w_u(\tilde{\omega})/\partial x\right)\ \left(\partial w_u(\tilde{\omega})/\partial y\right)\ \left(\partial u_l(\tilde{\omega})/\partial x\right)\ \left(\partial u_l(\tilde{\omega})/\partial y\right) \\ &\left(\partial v_l(\tilde{\omega})/\partial x\right)\ \left(\partial v_l(\tilde{\omega})/\partial y\right)\ \left(\partial w_l(\tilde{\omega})/\partial x\right)\ \left(\partial w_l(\tilde{\omega})/\partial y\right)]. \end{aligned} \tag{10}$$

The details of $\left[H\left(\tilde{\omega}\right)\right]$ is not given here for brevity [47], while it can be readily obtained based on the form of $\left\{\varepsilon\left(\tilde{\omega}\right)\right\}$ provided in equation (10).

2.2. First-order shear deformation theory (FSDT)

According to the first-order shear deformation theory, the stochastic displacement field can be expressed as [51]

$$u(x,y,z)(\tilde{\omega}) = u_0(x,y)(\tilde{\omega}) - z\theta_x(x,y)(\tilde{\omega}) \tag{11}$$

$$v(x,y,z)(\tilde{\omega}) = v_0(x,y)(\tilde{\omega}) - z\theta_y(x,y)(\tilde{\omega}) \tag{12}$$

$$w(x,y,z)\left(\tilde{\omega}\right) = w_0\left(x,y\right)\left(\tilde{\omega}\right) = w\left(x,y\right)\left(\tilde{\omega}\right) \tag{13}$$

where the stochastic displacement in *x*, *y*, and *z*-direction is represented by $u\left(\tilde{\omega}\right)$, $v\left(\tilde{\omega}\right)$ and $w\left(\tilde{\omega}\right)$ respectively, and the displacement at mid-plane in *x*, *y*, and *z*-direction is represented by $u_0\left(\tilde{\omega}\right)$, $v_0\left(\tilde{\omega}\right)$ and $w_0\left(\tilde{\omega}\right)$ respectively. The rotation in the direction of *x* and *y* direction is represented by $\theta_x\left(\tilde{\omega}\right)$ and $\theta_y\left(\tilde{\omega}\right)$ respectively. The constitutive equations are as follows:

$$\left\{F\left(\tilde{\omega}\right)\right\} = [\,\dot{D}\left(\tilde{\omega}\right)]\left\{\varepsilon\left(\tilde{\omega}\right)\right\} \tag{14}$$

where

$$\left\{F\left(\tilde{\omega}\right)\right\} = \left\{\dot{N}_x\left(\tilde{\omega}\right), \dot{N}_y\left(\tilde{\omega}\right), \dot{N}_{xy}\left(\tilde{\omega}\right), \dot{M}_x\left(\tilde{\omega}\right), \dot{M}_y\left(\tilde{\omega}\right), \dot{M}_{xy}\left(\tilde{\omega}\right), \dot{Q}_x\left(\tilde{\omega}\right), \dot{Q}_y\left(\tilde{\omega}\right)\right\}^T$$

$$\left\{F\left(\tilde{\omega}\right)\right\} = \left[\int_{-h/2}^{h/2} \left\{\sigma_x\left(\tilde{\omega}\right), \sigma_y\left(\tilde{\omega}\right), \tau_{xy}\left(\tilde{\omega}\right), \sigma_{xz}\left(\tilde{\omega}\right), \sigma_{yz}\left(\tilde{\omega}\right), \tau_{xyz}\left(\tilde{\omega}\right), \tau_{xz}\left(\tilde{\omega}\right), \tau_{yz}\left(\tilde{\omega}\right)\right\} dz\right]^T$$

and strain $\left\{\varepsilon\left(\tilde{\omega}\right)\right\} = \left\{\varepsilon_x\left(\tilde{\omega}\right), \varepsilon_y\left(\tilde{\omega}\right), \varepsilon_{xy}\left(\tilde{\omega}\right), k_x\left(\tilde{\omega}\right), k_y\left(\tilde{\omega}\right), k_{xy}\left(\tilde{\omega}\right), \gamma_x\left(\tilde{\omega}\right), \gamma_y\left(\tilde{\omega}\right)\right\}^T$

$$[\dot{D}(\tilde{\omega})] = \begin{bmatrix} \dot{A}_{11}(\tilde{\omega}) & \dot{A}_{12}(\tilde{\omega}) & \dot{A}_{16}(\tilde{\omega}) & \dot{B}_{11}(\tilde{\omega}) & \dot{B}_{12}(\tilde{\omega}) & \dot{B}_{16}(\tilde{\omega}) & 0 & 0 \\ \dot{A}_{12}(\tilde{\omega}) & \dot{A}_{22}(\tilde{\omega}) & \dot{A}_{26}(\tilde{\omega}) & \dot{B}_{12}(\tilde{\omega}) & \dot{B}_{22}(\tilde{\omega}) & \dot{B}_{26}(\tilde{\omega}) & 0 & 0 \\ \dot{A}_{16}(\tilde{\omega}) & \dot{A}_{26}(\tilde{\omega}) & \dot{A}_{66}(\tilde{\omega}) & \dot{B}_{16}(\tilde{\omega}) & \dot{B}_{26}(\tilde{\omega}) & \dot{B}_{66}(\tilde{\omega}) & 0 & 0 \\ \dot{B}_{11}(\tilde{\omega}) & \dot{B}_{12}(\tilde{\omega}) & \dot{B}_{16}(\tilde{\omega}) & \dot{D}_{11}(\tilde{\omega}) & \dot{D}_{12}(\tilde{\omega}) & \dot{D}_{16}(\tilde{\omega}) & 0 & 0 \\ \dot{B}_{12}(\tilde{\omega}) & \dot{B}_{22}(\tilde{\omega}) & \dot{B}_{26}(\tilde{\omega}) & \dot{D}_{12}(\tilde{\omega}) & \dot{D}_{22}(\tilde{\omega}) & \dot{D}_{26}(\tilde{\omega}) & 0 & 0 \\ \dot{B}_{16}(\tilde{\omega}) & \dot{B}_{26}(\tilde{\omega}) & \dot{B}_{66}(\tilde{\omega}) & \dot{D}_{16}(\tilde{\omega}) & \dot{D}_{26}(\tilde{\omega}) & \dot{D}_{66}(\tilde{\omega}) & 0 & 0 \\ 0 & 0 & 0 & 0 & 0 & 0 & \dot{S}_{44}(\tilde{\omega}) & \dot{S}_{45}(\tilde{\omega}) \\ 0 & 0 & 0 & 0 & 0 & 0 & \dot{S}_{45}(\tilde{\omega}) & \dot{S}_{55}(\tilde{\omega}) \end{bmatrix} \tag{15}$$

Here, $[\dot{D}(\tilde{\omega})]$ is the elastic stiffness matrix. Its elements can be expressed as:

$$\begin{gathered} \left[\dot{A}_{ij}(\tilde{\omega}),\dot{B}_{ij}(\tilde{\omega}),\dot{D}_{ij}(\tilde{\omega})\right] = \sum_{k=1}^{n}\int_{z_{k-1}}^{z_k}\left[\left\{\tilde{Q}_{ij}(\tilde{\omega})_{0n}\right\}\right]_k\left[1,z,z^2\right]dz \\ i,j=1,2,6 \\ [\dot{S}_{ij}(\tilde{\omega})] = \sum_{k=1}^{n}\int_{z_{k-1}}^{z_k}\dot{\alpha}_s\left[\left\{\tilde{Q}_{ij}(\tilde{\omega})_{0n}\right\}\right]_k dz \\ i,j=4,5 \end{gathered} \tag{16}$$

where, $\dot{\alpha}_s$ is the shear correction factor and $\left\{\tilde{Q}_{ij}(\tilde{\omega})_{0n}\right\}$ are the elements of off-axis elastic constant matrix and is expressed as

$$\begin{gathered} [\tilde{Q}_{ij}(\tilde{\omega})]_{off} = [\dot{T}_1(\tilde{\omega})]^{-1}[\tilde{Q}_{ij}(\tilde{\omega})]_{on}[\dot{T}_1(\tilde{\omega})]^{-T} \\ i,j=1,2,6 \\ [\tilde{Q}_{ij}(\tilde{\omega})]_{off} = [\dot{T}_2(\tilde{\omega})]^{-1}[\tilde{Q}_{ij}(\tilde{\omega})]_{on}[\dot{T}_2(\tilde{\omega})]^{-T} \\ i,j=4,5 \end{gathered} \tag{17}$$

$$[\dot{T}_1(\tilde{\omega})] = \begin{bmatrix} \dot{m}^2(\tilde{\omega}) & \dot{n}^2(\tilde{\omega}) & 2\dot{m}(\tilde{\omega})\dot{n}(\tilde{\omega}) \\ \dot{n}^2(\tilde{\omega}) & \dot{m}^2(\tilde{\omega}) & -2\dot{m}(\tilde{\omega})\dot{n}(\tilde{\omega}) \\ -\dot{m}(\tilde{\omega})\dot{n}(\tilde{\omega}) & \dot{m}(\tilde{\omega})\dot{n}(\tilde{\omega}) & \dot{m}^2(\tilde{\omega})-\dot{n}^2(\tilde{\omega}) \end{bmatrix} and\, [\dot{T}_2(\tilde{\omega})] = \begin{bmatrix} \dot{m}(\tilde{\omega}) & -\dot{n}(\tilde{\omega}) \\ \dot{n}(\tilde{\omega}) & \dot{m}(\tilde{\omega}) \end{bmatrix} \tag{18}$$

In which $\dot{m}(\tilde{\omega}) = sin\theta(\tilde{\omega})$ and $\dot{n}(\tilde{\omega}) = cos\theta(\tilde{\omega})$, while $\theta(\tilde{\omega})$ is the stochastic fiber orientation angle.

$$[\tilde{Q}_{ij}(\tilde{\omega})]_{on} = \begin{bmatrix} \tilde{Q}_{11}(\tilde{\omega}) & \tilde{Q}_{12}(\tilde{\omega}) & 0 \\ \tilde{Q}_{12}(\tilde{\omega}) & \tilde{Q}_{22}(\tilde{\omega}) & 0 \\ 0 & 0 & \tilde{Q}_{66}(\tilde{\omega}) \end{bmatrix}$$
$$i, j = 1,2,6 \tag{19}$$
$$[\tilde{Q}_{ij}(\tilde{\omega})]_{on} = \begin{bmatrix} \tilde{Q}_{44}(\tilde{\omega}) & \tilde{Q}_{45}(\tilde{\omega}) \\ \tilde{Q}_{45}(\tilde{\omega}) & \tilde{Q}_{55}(\tilde{\omega}) \end{bmatrix}$$
$$i, j = 4,5$$

$\tilde{Q}_{ij}(\tilde{\omega})$ are the material constants in the material axes of the layer, given as:

$$\begin{aligned} &\tilde{Q}_{11}(\tilde{\omega}) = \frac{E_1(\tilde{\omega})}{1-\nu_{12}(\tilde{\omega})\nu_{21}(\tilde{\omega})}, \; \tilde{Q}_{22}(\tilde{\omega}) = \frac{E_2(\tilde{\omega})}{1-\nu_{12}(\tilde{\omega})\nu_{21}(\tilde{\omega})}, \; \tilde{Q}_{12}(\tilde{\omega}) = \frac{\nu_{21}(\tilde{\omega})E_1(\tilde{\omega})}{1-\nu_{12}(\tilde{\omega})\nu_{21}(\tilde{\omega})}, \\ &\tilde{Q}_{66}(\tilde{\omega}) = G_{12}(\tilde{\omega}), \qquad \tilde{Q}_{55}(\tilde{\omega}) = G_{13}(\tilde{\omega}), \qquad \tilde{Q}_{44}(\tilde{\omega}) = G_{23}(\tilde{\omega}), \end{aligned} \tag{20}$$

where $E(\tilde{\omega})$ is the modulus of elasticity and $G(\tilde{\omega})$ is shear modulus.

2.3. Free vibration analysis

Considering Hamilton's principle with stochasticity, it can be expressed as,

$$\delta H(\tilde{\omega}) = \int_{p_i}^{p_f} [\delta T(\tilde{\omega}) - \delta U(\tilde{\omega}) - \delta W(\tilde{\omega})]\, dp = 0 \tag{21}$$

where $T(\tilde{\omega})$ and $W(\tilde{\omega})$ are the stochastic kinetic energy and the stochastic work done by conservative and non-conservative forces, respectively. For free vibration analysis (i.e., $\delta W(\tilde{\omega})$ = 0), the stochastic energy functional for Hamilton's principle is the Lagrangian (L_f) which includes stochastic kinetic energy ($T(\tilde{\omega})$) in addition to stochastic potential strain energy ($U(\tilde{\omega})$) of an elastic body. The expression for stochastic kinetic energy of an element is expressed as

$$T(\tilde{\omega}) = \frac{1}{2}\left\{\dot{\delta}_e(\tilde{\omega})\right\}^T \left[M_e(\tilde{\omega})\right]\left\{\dot{\delta}_e(\tilde{\omega})\right\} \tag{22}$$

The stochastic potential strain energy for an element of a plate can be expressed as [51],

$$U(\tilde{\omega}) = U_1(\tilde{\omega}) + U_2(\tilde{\omega}) = \frac{1}{2}\left\{\dot{\delta}_e(\tilde{\omega})\right\}^T \left[\dot{K}_e(\tilde{\omega})\right]\left\{\dot{\delta}_e(\tilde{\omega})\right\} + \frac{1}{2}\left\{\dot{\delta}_e(\tilde{\omega})\right\}^T \left[\dot{K}_{\sigma e}(\tilde{\omega})\right]\left\{\dot{\delta}_e(\tilde{\omega})\right\} \tag{23}$$

The Langrange's equation of motion with stochasticity is stated as,

$$\frac{d}{dt}\left[\frac{\partial L_f(\tilde{\omega})}{\partial \dot{\delta}_e(\tilde{\omega})}\right] - \left[\frac{\partial L_f(\tilde{\omega})}{\partial \dot{\delta}_e(\tilde{\omega})}\right] = \left\{\dot{F}_e(\tilde{\omega})\right\} \tag{24}$$

where $\{\dot{F}_e(\tilde{\omega})\}$ is the stochastic applied external force vector of an element (for free vibration $\{\dot{F}_e(\tilde{\omega})\}$ is zero) and L_f is the Lagrangian function. Substituting $\partial L_f(\tilde{\omega}) = T(\tilde{\omega}) - U(\tilde{\omega})$, and the corresponding expressions for $T(\tilde{\omega})$ and $U(\tilde{\omega})$ in Lagrange's equation, the stochastic dynamic equilibrium equation for each element can be obtained [42]. Hence, the generalized stochastic dynamic equilibrium equation [51] can be stated as,

$$[M(\tilde{\omega})]\{\ddot{\delta}(\tilde{\omega})\} + ([K_e(\tilde{\omega})] + [K_{\sigma e}(\tilde{\omega})])\{\delta(\tilde{\omega})\} = \{F(\tilde{\omega})\} \quad (25)$$

where $\{\delta(\tilde{\omega})\}$ is the global stochastic displacement vector, $[M(\tilde{\omega})]$ is global stochastic mass matrix, while $[K_e(\tilde{\omega})]$ and $[K_{\sigma e}(\tilde{\omega})]$ represent the respective global stochastic matrices corresponding to elastic stiffness, and geometric stiffness. $\{F(\tilde{\omega})\}$ indicates the stochastic externally applied force vector. These global matrices are essentially obtained by assembling elementary-level matrices. In the present study, the effect of initial stress is not considered. Hence, the geometric stiffness matrix can be neglected from eq. (25). Considering free vibration, the dynamic equilibrium equation of motion can be expressed as,

$$[M(\tilde{\omega})]\{\ddot{\delta}(\tilde{\omega})\} + [K(\tilde{\omega})]]\{\delta(\tilde{\omega})\} = 0 \quad (26)$$

For the present analysis, it is considered that the stochastic displacement vector $\{\delta(\tilde{\omega})\}$ contains both static and dynamic term [$\{\delta(\tilde{\omega})\} = \{\delta_s(\tilde{\omega})\} + \{\delta_p(\tilde{\omega})\}$, where $\{\delta_p(\tilde{\omega})\}$ is a small linear time-dependent disturbance about the static displaced position $\{\delta_s(\tilde{\omega})\}$. Neglecting the static displaced position, the stochastic equation of motion can be expressed as,

$$[M(\tilde{\omega})]\{\ddot{\delta}_p(\tilde{\omega})\} + [K(\tilde{\omega})]\{\delta_p(\tilde{\omega})\} = 0 \quad (27)$$

In eq. (27), the stochastic displacement $\{\delta_p(\tilde{\omega})\}$ is a function of time and space. In natural frequency analysis, the space and time coordinates of stochastic displacement function can be expressed as,

$$\{\delta_p(\tilde{\omega})\} = A' e^{i\omega(\tilde{\omega})t}\{\Phi(\tilde{\omega})\} \quad (28)$$

Therefore,

$$\{\ddot{\delta}_p(\tilde{\omega})\} = -A'\{\omega(\tilde{\omega})\}^2 e^{i\omega(\tilde{\omega})t}\{\Phi(\tilde{\omega})\} \quad (29)$$

On substituting the values of $\left\{\delta_p\left(\tilde{\omega}\right)\right\}$ and $\left\{\ddot{\delta}_p\left(\tilde{\omega}\right)\right\}$ in eq. (27), the modified equation becomes

$$A'e^{i\omega(\tilde{\omega})t}(-\{\omega(\tilde{\omega})\}^2[M(\tilde{\omega})]\{\Phi\}+[K(\tilde{\omega})]\{\Phi(\tilde{\omega})\})=0 \tag{30}$$

As $A'e^{i\omega t}\neq 0$

$$\{\omega(\tilde{\omega})\}^2[M(\tilde{\omega})]\{\Phi(\tilde{\omega})\}=[K(\tilde{\omega})]\{\Phi(\tilde{\omega})\} \tag{31}$$

Here $\omega\left(\tilde{\omega}\right)$ represents the stochastic natural frequencies. Now, utilizing the standard eigen value problem [38] $\omega(\tilde{\omega})$ can be evaluated. QR iteration algorithms can be employed to solve the equation and it can be stated as,

$$[A(\tilde{\omega})]\,\{\Phi(\tilde{\omega})\}=\lambda(\tilde{\omega})\{\Phi(\tilde{\omega})\} \tag{32}$$

$$\text{where}\quad [A(\tilde{\omega})]=[K(\tilde{\omega})]^{-1}[M(\tilde{\omega})]$$

$$\text{and}\quad \lambda(\tilde{\omega})=1/(\omega\left(\tilde{\omega}\right))^2 \tag{33}$$

2.4. Finite element formulation

The deterministic finite element formulation is implemented considering an isoperimetric quadratic element with eight nodes wherein each node has five degrees of freedom (three translations and two rotations). The polynomial shape functions having coordinates (ξ, η, ζ) can be employed, relating the nodal values of displacements to the generalized displacements (as shown in Figure 2 and Figure 3). For the present analysis, the interpolation of the polynomial can be expressed as,

$$\hat{u}(\xi,\eta)=D_0+D_1\xi+D_2\eta+D_3\xi^2+D_4\xi\eta+D_5\eta^2+D_6\xi^2\eta+D_7\xi\eta^2 \tag{34}$$

where, $D_0, D_1, ...D_7$ are the generalized DOF. The shape functions S_i can be expressed as,

$$S_i=\frac{1}{4}\left(1+\xi\xi_i\right)\left(\xi\xi_i+\eta\eta_i-1\right)\left(1+\eta\eta_i\right)\quad\text{, where } i=1,2,3,4$$

$$S_i=\frac{1}{2}\left(1+\eta\eta_i\right)\left(1-\xi^2\right)\quad\text{, where } i=5,7 \tag{35}$$

$$S_i=\frac{1}{2}\left(1+\xi\xi_i\right)\left(1-\eta^2\right)\quad\text{, where } i=6,8$$

where, ξ, η represent natural coordinates. The shape functions accuracy is stated as,

$$\sum_{i=1}^{8} S_i = 1, \quad \sum_{i=1}^{8} \frac{\partial S_i}{\partial \xi} = 0 \quad \text{and} \quad \sum_{i=1}^{8} \frac{\partial S_i}{\partial \eta} = 0 \tag{36}$$

At any point, the coordinates (x, y) can be represented as

$$x = \sum_{i=1}^{8} S_i\, x_i \quad \text{and} \quad y = \sum_{i=1}^{8} S_i\, y_i \tag{37}$$

The displacement at any point can be shown as

$$u = \sum_{i=1}^{8} S_i\, u_i\,, \quad v = \sum_{i=1}^{8} S_i\, v_i\,, \quad w = \sum_{i=1}^{8} S_i\, w_i\,, \quad \theta_x = \sum_{i=1}^{8} S_i\, \theta_{xi}\,, \theta_y = \sum_{i=1}^{8} S_i\, \theta_{yi} \tag{38}$$

$$\text{and} \quad \begin{bmatrix} S_{i,x} \\ S_{i,y} \end{bmatrix} = [J]^{-1} \begin{bmatrix} S_{i,\xi} \\ S_{i,\eta} \end{bmatrix} \tag{39}$$

where $[J] = \begin{bmatrix} x_\zeta & y_\zeta \\ x_\eta & y_\eta \end{bmatrix}$ is the Jacobian matrix.

The elemental potential energy (U_e) of deformation is stated as,

$$U_e = \frac{1}{2} \int_A \{\varepsilon\}^T\ [D]\ \{\varepsilon\}\ dA \tag{40}$$

$$\text{where}\ \{\varepsilon\} = [B]\ \{\delta_e\}\ = [\,[B_1] \,.\,.\,.\,.\,.\,.\,.\, [B_8]]\, \{\delta_e\} \tag{41}$$

$$\{\delta_e\} = [u^o{}_1\ \ v^o{}_1\ \ w^o{}_1\ \ \theta^o{}_{x1}\ \ \theta^o{}_{y1}\ \ldots\ldots\ u^o{}_8\ \ v^o{}_8\ \ w^o{}_8\ \ \theta^o{}_{x8}\ \ \theta^o{}_{y8}]^T \tag{42}$$

Here $u^o{}_1$, $v^o{}_1$, $w^o{}_1$, $\theta^o{}_{x1}$, $\theta^o{}_{y1}$ … $u^o{}_8$, $v^o{}_8$, $w^o{}_8$, $\theta^o{}_{x8}$, $\theta^o{}_{y8}$ are mid-surface displacements. Thus we get

$$U_e = \frac{1}{2} \int_{-a'_o/2}^{a'_o/2} \int_{-b'_o/2}^{b'_o/2} \{\delta_e\}^T\ [B]^T\ [D]\ [B]\ \{\delta_e\}\ dx\ dy\ = \frac{1}{2}\ \{\delta_e\}^T\ [K_e]\ \{\delta_e\} \tag{43}$$

where a'_o describes the plate element length and b'_o describes the plate element width. The element stiffness matrix is expressed as

$$[K_e]\ = \int_{-a'_o/2}^{a'_o/2} \int_{-b'_o/2}^{b'_o/2} [B]^T\ [D]\ [B]\ dx\, dy\ \text{where}\ dx\, dy\ = [J]\, d\xi\ d\eta \tag{44}$$

$$\text{Thus,}\ [K_e]\ = \int_{-1}^{1} \int_{-1}^{1} [B]^T\ [D]\ [B]\ d\xi\ d\eta \tag{45}$$

$$[B_i]=\begin{bmatrix} S_{i,x} & O & O & O & O \\ O & S_{i,y} & S_i/R_y & O & O \\ S_{i,y} & S_{i,x} & 2S_i/R_{xy} & O & O \\ O & O & O & -S_{i,x} & O \\ O & O & O & O & -S_{i,y} \\ O & O & O & -S_{i,y} & -S_{i,x} \\ O & O & -S_{i,x} & -S_i & O \\ O & O & -S_{i,y} & O & -S_i \end{bmatrix} (i\text{=1 to 8}) \quad (46)$$

Both the translatory and rotatory inertia terms are included in the generalized inertia matrix per unit

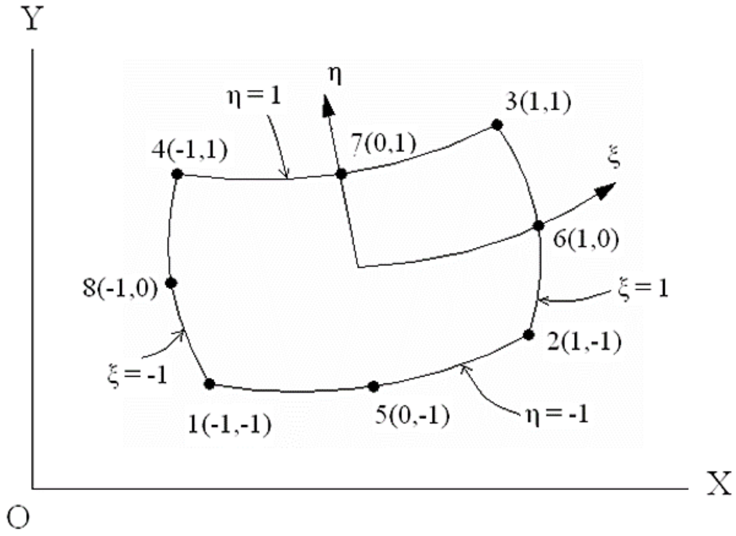

Fig. 2: An isoparametric quadratic element represented in XY space

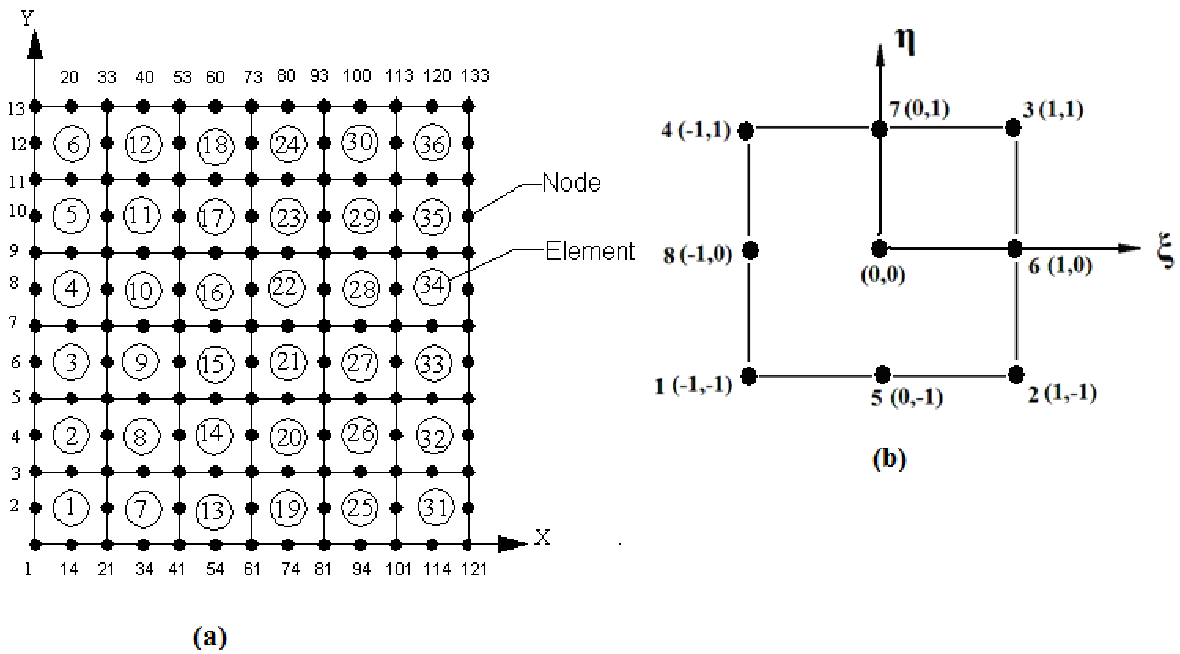

Fig. 3: Finite element discretization of plane area (a) 6 x 6 mesh (b) An element in ξ - η space

area. Mass per unit area (P) is represented as

$$P = \sum_{k=1}^{n=8} \int_{z_{k-1}}^{z_k} \rho \; dz \tag{47}$$

where, ρ is mass density and moment of inertia per unit area (I_1) is stated as,

$$I_1 = \sum_{k=1}^{n=8} \int_{z_{k-1}}^{z_k} z\,\rho \; dz. \tag{48}$$

The element mass matrix is expressed as,

$$\left[M_e\right] = \int_{\varphi} [S]^T \left[P\right] \left[S\right] d\varphi \tag{49}$$

where

$$\left[S\right] = \begin{bmatrix} \langle S_i \rangle & & & & \\ & \langle S_i \rangle & & & \\ & & \langle S_i \rangle & & \\ & & & \langle S_i \rangle & \\ & & & & \langle S_i \rangle \end{bmatrix}, \tag{50}$$

and

$$\left[P\right] = \begin{bmatrix} P & & & & \\ & P & & & \\ & & P & & \\ & & & I & \\ & & & & I \end{bmatrix}. \tag{51}$$

There will be the existence of in-plane stresses at mid-point because of the rotation. Therefore the new geometric stiffness matrix is stated as,

$$[K_{\sigma e}] = \int_{\Phi} [S]^T \; [M_{\sigma}][S] d\Phi \tag{52}$$

where the derivative of shape functions are stored in $[S]$ and $[M_\sigma]$ stores the initial in-plane stress resultant matrix due to the rotation. It may be noted that the above equation is provided for the sake of completeness of the formulation. Geometric stiffness has not been considered in the current paper for numerical analysis.

2.5. Gaussian Process Regression (GPR) based machine learning

For the present study, the surrogate adopted for modifying the FSDT theory is GPR [37, 63, 64]. Such GPR based machine learning algorithm can create an efficient computational mapping between a set of input and output parameters [48-50]. In case of GPR, a random variables collection exists, which are extracted from a finite number of consistent joint Gaussian distributions. In general, we can define GP by a mean function $f(\bar{a})$ which is a vector and a covariance function $y(\bar{b},\bar{b}')$ which is matrix. Gaussian distribution is there for vectors while GP is there for functions [39, 40]. Let there be function l, distributed as a GP and having $\bar{f}$ as a mean function and $\bar{y}$ as a covariance function

$$l \approx GP(\bar{f},\bar{y}) \tag{53}$$

For random function $f(\bar{b})$, it is the argument $\bar{b}$ which behaves like index set i.e. for each input $\bar{b}$, there exist a random variable $f(\bar{b})$, which is the value of probabilistic function l at that location. The complete operational procedure is described in figure 4. To forecast the unknown test variables, let l be the recognized function value of the training set and l^* be the set of function values equivalent to the test set inputs (B^*) . The joint distribution of everything can be given by

$$\begin{vmatrix} l \\ l^* \end{vmatrix} \approx GP\left(\begin{bmatrix} \bar{f} \\ \bar{f}^* \end{bmatrix}, \begin{bmatrix} \bar{y} & \bar{y}^* \\ \bar{y}^{*T} & \bar{y}^{**} \end{bmatrix}\right) \tag{54}$$

where for the training means $\bar{f} = f(\bar{b}_i),\ i = 1,.........n.$ and for the test means $\bar{f}^*$. Covariances for various sets are as follows:

Covariance	**set**
$\bar{y}$	training set
$\bar{y}^*$	training-test set
$\bar{y}^{**}$	test set

The value of training set l and the conditional distribution of l^* can be stated as,

$$l/l^* \approx GP(\bar{f}^* + \bar{y}^{*T}\bar{y}^{-1}(l-\bar{f}), \bar{y}^{**} - \bar{y}^{*T}\bar{y}^{-1}\bar{y}^*) \tag{55}$$

For a specific set of test cases, the above equation represents the posterior. It can be verified that

$$
\begin{aligned}
& l/D \approx GP(\bar{f}_D, \bar{y}_D), \\
& f_D(\bar{b}) = f(\bar{b}) + \bar{y}(B,\bar{b})^T \bar{y}^{-1}(l - \bar{f}) \\
& c_D(\bar{b},\bar{b}') = l(\bar{b},\bar{b}') - \bar{y}(B,\bar{b})^T \bar{y}^{-1}\bar{y}(B,\bar{b}')
\end{aligned}
\tag{56}
$$

where $\bar{y}(B,\bar{b})$ denotes the covariance vector for $\bar{b}$ and for each training case. For GP prediction, these are the central equations. As it is a non-parametric model, the behavior of marginal likelihood is opposite to that of the expectations compared with parametric models. It eases the model fitment with the training data, producing a mean function that agrees exactly with the training points. Here, there is an automatic trade-off between penalty and data-fit. No weighting parameters are required. This feature makes the training process simple.

2.6. Modified first-order shear deformation theory (mFSDT) based stochastic analysis

In the present stochastic analysis, Gaussian process regression (GPR) is integrated with the original FSDT to obtain a new framework of modified FSDT (mFSDT). Essentially, we augment the accuracy of FSDT to the level of HOZT by bridging their difference through the GP based mapping, while keeping the computational expenses similar to that of the original FSDT. It may be noted in this context that, in principle, any other machine learning model can be adopted in this framework based on their efficiency and prediction capability. For the formation of mFSDT, the following steps are performed (refer to figure 4(a)). Firstly, a set of outputs are obtained (here, natural frequencies corresponding to first and second modes of vibration) for a given sample size with a definite number of input parameters; let it be *N* (here, the stochastic input parameters considered are various material properties). Let *Z* be the input matrix for which a set of outputs are obtained. Firstly the outputs are obtained using FSDT theory; let it be f_1. Then, using the same set of the input matrix, i.e. *Z*, which was used for FSDT, we obtain the output by using HOZT; let the new output obtain be f_1'. Then we calculate the error ($e= f_1'- f_1$). After that, form a surrogate (here, we have considered GPR as a surrogate model) between *Z* (input space) and *e* (output space). Let e' be the predictor obtained by utilizing GPR. Thus, for any arbitrary input sample, the result corresponding to mFSDT can be obtained by adding the outcome of FSDT (obtained using FSDT based FE simulation) to the corresponding predicted error e' (obtained using GPR). If the GPR model is accurate enough, the results of mFSDT would be equivalent to that of HOZT, while the computational expense required for evaluating the natural frequencies remains the same as FSDT. Now construct another set of input matrices, different from that of the initial *Z* matrix, and then obtain new output for that using FSDT and HOZT; let these be defined as f_F and f_H, respectively. Then obtain percentage errors between HOZT and FSDT, let it be represented by *a* (where $a = ((f_H - f_F) / f_H) \times 100$), and obtain percentage errors between HOZT and mFSDT ($f_H + e'$), let it be represented by *b* (where, $b = ((f_H - (f_F + e') / f_H) \times 100$). Check whether $a > b$; if yes then this shows that the adopted mFSDT provides outputs with lesser error compared to the original FSDT.

The proposed framework of mFSDT can achieve a significant level of cumulative computational efficiency when a large number of simulations are required to be carried out, such as Monte Carlo simulation (MCS) based stochastic analysis. In the present study, concerning laminated composite and sandwich structures, the following cases of stochasticity are considered to analyze the effect of inevitable source uncertainty in material properties:

I. Source uncertainty in material properties

$$f_1\{E(\tilde{\omega}), G(\tilde{\omega}), \rho(\tilde{\omega}), \mu(\tilde{\omega})\} = \varphi[\{E(z)\}(\tilde{\omega}), \{G(z)\}(\tilde{\omega}), \{\rho(z)\}(\tilde{\omega}), \{\mu(z)\}(\tilde{\omega})]$$

II. Effect of material uncertainty in the variation of the laminate thickness (t)

$$f_2(t, \tilde{\omega}) = \varphi[\{E(z)\}(\tilde{\omega}), \{G(z)\}(\tilde{\omega}), \{\mu(z)\}(\tilde{\omega}), \{\rho(z)\}(\tilde{\omega})]$$

III. Effect of material uncertainty in the variation of E_1/E_2 ratio (degree of orthotropy)

$$f_3(\frac{E_1}{E_2}, \tilde{\omega}) = \varphi[\{E(z)\}(\tilde{\omega}), \{G(z)\}(\tilde{\omega}), \{\mu(z)\}(\tilde{\omega}), \{\rho(z)\}(\tilde{\omega})]$$

In the above expressions φ depicts the MCS operator and $\tilde{\omega}$ is used to indicate the notion of uncertainty associated with a particular parameter. The present study deals with the stochastic input parameter variation obtained from random uniform distributions in the form of percentage deviation ($\tilde{\omega} = c$) with respect to the corresponding deterministic nominal values. Note that, while other distributions can be adopted for the stochastic input parameters, we adopt the random uniform distributions here to capture the stochastic bounds of the response quantities of interest. If not mentioned otherwise, we have considered c = 10% for the subsequent numerical results (according to normal industry standards).

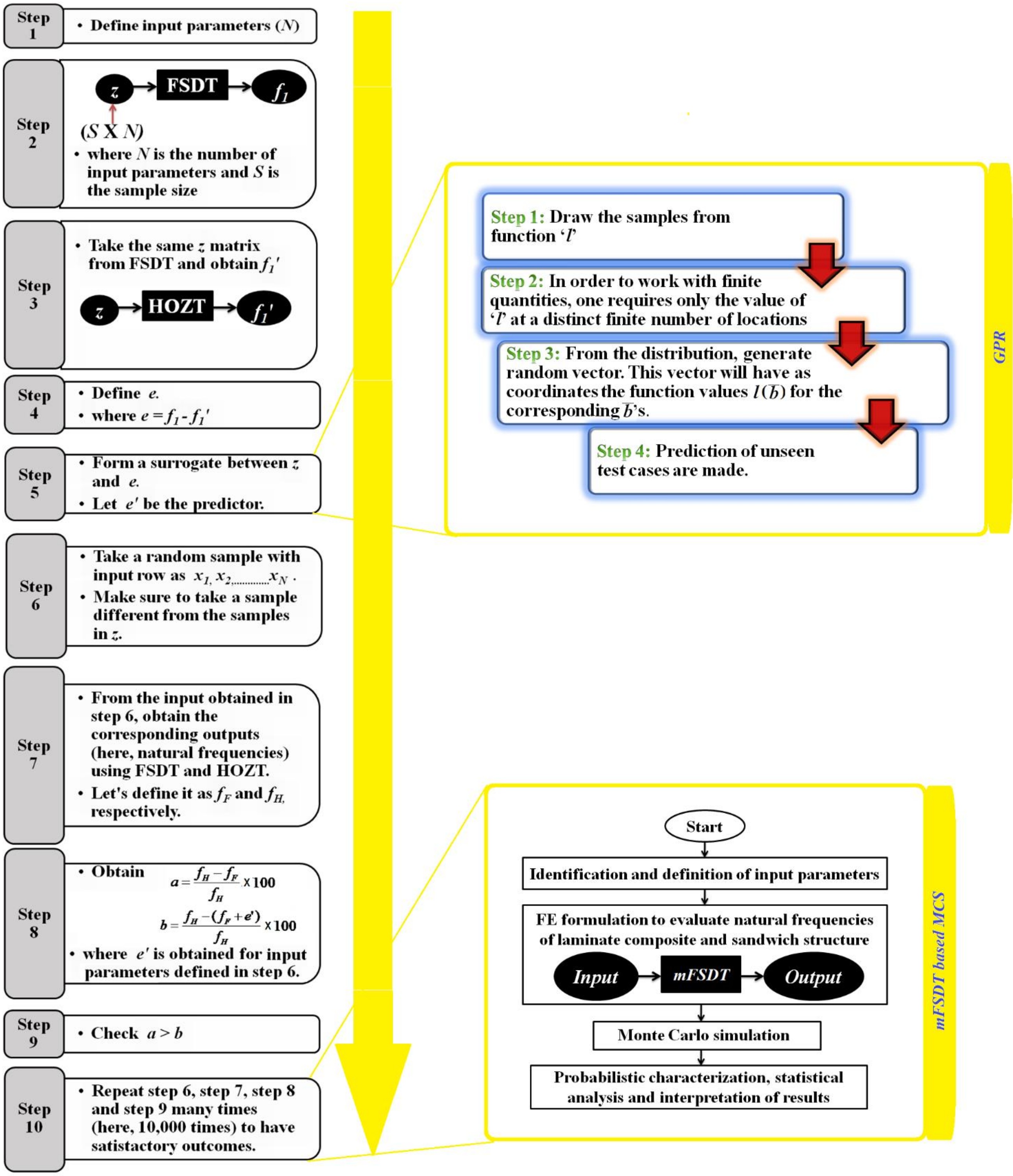

Fig. 4: Flowchart showing complete methodology for developing modified FSDT (mFSDT) and validating the results obtained by comparing it with HOZT. The inset figure corresponding to Step 5 shows the algorithm employed while performing GPR based surrogate modeling. The inset figure corresponding to Step 10 shows the mFSDT based probabilistic analysis framework by employing Monte Carlo simulation (MCS).

3. Results and discussion

In the present study, the investigation is conducted by studying the influence of various critical parameters on the natural frequencies of laminated composite and sandwich structures, firstly by following a deterministic framework, and then in the stochastic domain. The first and second natural frequencies (denoted by NF_1 and NF_2, respectively) are considered as output here. For obtaining the probabilistic results of natural frequencies, the MCS is carried out in conjunction with the proposed mFSDT framework.

For checking the accuracy of the present numerical framework, two different validations are shown. First validation shows the accuracy of the deterministic FE code. For that, the FE codes of both HOZT and FSDT based analysis of laminated composite and sandwich structures are validated with the results of the past literature. The second validation is for the proposed mFSDT algorithm. The mFSDT code is validated with the HOZT results to show the accuracy and prediction ability of this newly developed algorithm.

We have considered a cantilever plate of dimension as l = 0.1 m, b = 0.1 m and t = 0.01 m with $0°$ skew angle unless otherwise mentioned, for both deterministic and stochastic natural frequency analyses. In the case of the sandwich plate, we have considered core thickness ($t_c = 0.008\ m$) and facesheet thickness $(t_f = 0.002\ m)$. Here the facesheet comprises laminated composites having four symmetric lamina (0°/90°/0°/90°/c/90°/0°/90°/0°) on both sides of the core. In case of the laminated composite plates, we consider (0°/90°/0°/90°/) ply configuration. Schematic representations of both the structures analyzed in the present study are provided in figure 1. Material properties [41] considered for the analysis are given below:

(a) core:

E_1 = E_2 = E_3 = 0.5 GPa, G_{12} = G_{13} = 0.4 GPa, G_{23} = 0.2 GPa, $\upsilon_{12} = \upsilon_{13} = \upsilon_{23} = \upsilon_{32} = 0.27$, $\upsilon_{21} = \upsilon_{31} = 0.006$, ρ =1000 kg/m^3

(b) laminated composite:

E_1 = 38.6 GPa, E_2 = E_3 = 8.27 GPa, G_{12} = G_{13} =4.14 GPa, G_{23} = 1.656 GPa, $\upsilon_{12} = \upsilon_{13} = \upsilon_{23} = \upsilon_{32} = 0.26$, $\upsilon_{21} = \upsilon_{31} = 0.006$, ρ =2600 kg/m^3.

We have presented results in the following subsections for both composite laminates and sandwich plates based on the deterministic and stochastic regimes. Note that conventional composite laminates can essentially be thought as a special case of the laminated composite and sandwich structures as presented in figure 1.

3.1. Deterministic analysis

For validation, the deterministic FE code is developed considering a cantilever plate, which is found to provide satisfactory results with a discretization of 6 x 6 mesh size (36 elements and 133 nodes) as shown in figure 3. A Mesh convergence study is performed for selecting optimized mesh size (refer to Table S2 of the supplementary material). The deterministic results obtained from the codes (HOZT and FSDT) are validated with that of the results presented in previous literature [42-45] (refer to Table 1 - 4), wherein it can be observed that the current results are in good agreement (here the accuracy may be slightly increased by considering finer meshes). After having confidence in the validity and accuracy of the FE code for HOZT and existing FSDT, the natural frequencies of laminated composites and sandwich structures(refer to figure 1) are investigated deterministically for various influencing parameters further to obtain deeper physical insights.

Table 1: Comparison of results (*NF*) obtained by the present study and that of Khandelwal [42]. Here, HOZT is considered for obtaining *NF* of laminated composite plates (0°/90°/90°/0°) in both the cases.

R	Mode	Present study (HOZT)	Khandelwal [42] (HOZT)	Error (%)
0.0	1	10.8260	10.8240	0.0180
	2	12.1710	12.1680	0.0240

Table 2: Comparison of results (*NF*) obtained by the present study and that of Kulkarni and Kapuria [43]. Here, HOZT is considered for obtaining *NF* of anti-symmetric laminates (90°/0°/90°/0°) in both the cases.

Skew angle	Mode	Present study (HOZT)	Kulkarni and Kapuria [43] (HOZT)	Error (%)
30^o	1	1.8889	1.9209	1.6650
	2	3.4827	3.5353	1.4870
	3	4.3019	4.3439	0.9660

Table 3: Comparison of results (*NF*) obtained by the present study and that of Thai [44]. Here, FSDT is considered for obtaining *NF* of cross-ply (0^o/90^o)s laminated composite plates (a = 5h) in both the cases.

E_1/ E_2	Mode	Present study (FSDT)	Thai [44] (FSDT)	Error (%)
3	1	6.1836	6.2085	0.4010
10	1	6.7634	6.9392	2.5330

Table 4: Comparison of results (*NF*) obtained by the present study and that of Mantari [45]. Here, FSDT is considered for obtaining *NF* of anti-symmetric (0^o/90^o /c/0^o/90^o) sandwich plates (a = b =1; a = h = 10) in both the cases.

t_c/ t_f	Mode	Present study (FSDT)	Mantari [45] (FSDT)	Error (%)
4	1	13.1749	13.3307	1.1687
10	1	14.5383	14.1454	2.7770

Table 5 shows the results obtained by varying the thickness of laminates, while table 6 shows the results for sandwich structures. The results obtained in the form of first (NF_1) and second (NF_2) natural frequencies show that on incrementing the thickness value of the laminates, the natural frequencies also increase for both laminated composite structures as well as for sandwich structures. The results are obtained using both HOZT and FSDT, and the differences in the results are shown in the form of error percentages. Table 7 presents the effect of variation in the degree of orthotropy on NF_1 and NF_2 of laminated composite plates, while Table 8 shows similar results for sandwich structures. It is witnessed that on incrementing the degree of orthotropy (E_1/ E_2 ratio), the value of natural frequencies decreases for both laminated composite structures as well as for sandwich structures. The results clearly show that there exist significant discrepancies between the predictions of FSDT and HOZT, wherein HOZT is believed to produce more accurate results. Through the introduction of mFSDT, we aim to minimize such discrepancies.

In the following subsection, we would concentrate on the accuracy of mFSDT first, followed by a stochastic analysis based on mFSDT for both composite laminates and sandwich structures. The effect of stochastic material properties would be investigated considering different critical parameters such as thickness and degree of orthotropy.

Table 5: Influence of thickness of laminates (t) on deterministic NF_1 and NF_2 of laminated composite plates. Here the percentage error is obtained with respect to HOZT.

Thickness of laminates (t) in meter	Theories	NF_1 (rad/s)	% error	NF_2 (rad/s)	% error
0.01	HOZT	24.5001	1.5760	48.5364	4.2800
	FSDT	24.1138		46.4572	
0.011	HOZT	26.4097	-0.4330	51.8740	1.5209
	FSDT	26.5243		51.0851	
0.012	HOZT	28.2092	-2.5700	54.9461	-1.3885
	FSDT	28.9345		55.7091	

Table 6: Influence of thickness of laminates (t) on deterministic NF_1 and NF_2 of sandwich plates. Here the percentage error is obtained with respect to HOZT.

Thickness of laminates (t) in meter	Theories	NF_1 (rad/s)	% error	NF_2 (rad/s)	% error
0.01	HOZT	11.7038	6.4600	23.8903	11.1500
	FSDT	10.9474		21.2257	
0.02	HOZT	13.2405	2.4000	26.0637	3.9310
	FSDT	12.9221		25.0390	
0.025	HOZT	14.6136	-1.6030	27.9217	-3.0280
	FSDT	14.8479		28.7673	

Table 7: Influence of E_1/E_2 ratio on deterministic NF_1 and NF_2 of laminated composite plates. Here the percentage error is obtained with respect to HOZT.

E_1/E_2 ratio	Theories	NF_1 (rad/s)	% error	NF_2 (rad/s)	% error
3	HOZT	25.4497	-0.6880	51.3488	7.350
	FSDT	25.6249		47.5102	
4	HOZT	24.8694	0.7200	49.6518	5.6240
	FSDT	24.6903		46.8591	
5	HOZT	24.5001	1.5760	48.5364	4.2800
	FSDT	24.1138		46.4572	

Table 8: Influence of E_1/E_2 ratio on deterministic NF_1 and NF_2 of sandwich plates. Here the percentage error is obtained with respect to HOZT.

E_1/E_2 ratio	Theories	NF_1 (rad/s)	% error	NF_2 (rad/s)	% error
3	HOZT	14.0402	9.9300	26.8788	4.6600
	FSDT	12.6423		25.6150	
4	HOZT	13.6174	-1.2652	26.0268	-1.5172
	FSDT	13.7897		26.4217	
5	HOZT	13.5599	-1.0450	25.9018	-1.7670

	FSDT	13.7017		26.3596	

3.2. *Stochastic analysis*

In this subsection, Tables 9-14 and Figures 5–16 present the detailed comparison of results between original FSDT and mFSDT with respect to HOZT for various parameters in laminated composite plates and sandwich structure. Tables 9-14 present the percentage error values (maximum, minimum and mean) between HOZT and original FSDT i.e. without modification, represented by *a*

Table 9: Percentage error for NF_1 and NF_2 obtained using original FSDT (without modification) and mFSDT (with modification) for different values of stochasticity (c) in case of laminated composite plates (for details about a and b refer to figure 4). Here the percentage error is obtained with respect to HOZT.

c	Theory	Natural frequencies	Maximum percentage error (%)	Minimum percentage error (%)	Mean percentage error (%)
1%	Without modifications (a)	First natural frequency	2.7264	0.4091	1.5769
	With modifications (b)	First natural frequency	0.6391	-0.6312	0.0156
	Without modifications (a)	Second natural frequency	5.5770	3.0041	4.2828
	With modifications (b)	Second natural frequency	0.8647	-0.8082	0.0155
3%	Without modifications (a)	First natural frequency	4.9881	-1.9664	1.5709
	With modifications (b)	First natural frequency	1.8873	-1.9174	0.0464
	Without modifications (a)	Second natural frequency	8.1170	0.3936	4.2731
	With modifications (b)	Second natural frequency	2.6265	-2.3990	0.0561
5%	Without modifications (a)	First natural frequency	7.2017	-4.3982	1.5568
	With modifications (b)	First natural frequency	3.1066	-3.2402	0.0750
	Without modifications (a)	Second natural frequency	10.5975	-2.2938	4.2539
	With modifications (b)	Second natural frequency	4.2052	-4.1656	0.0744

Table 10: Percentage error for NF_1 and NF_2 obtained using original FSDT (without modification) and mFSDT (with modification) for different values of stochasticity (c) in case of sandwich plates (for details about a and b refer to figure 4). Here the percentage error is obtained with respect to HOZT.

c	Theory	Natural frequencies	Maximum percentage error (%)	Minimum percentage error (%)	Mean percentage error (%)
1%	Without modifications (a)	First natural frequency	-0.1757	-2.2926	-1.2604
	With modifications (b)	First natural frequency	0.5222	-0.5414	0.0004
	Without modifications (a)	Second natural frequency	-0.2718	-2.7642	-1.5081
	With modifications (b)	Second natural frequency	0.8237	-0.8325	0.0033
3%	Without modifications (a)	First natural frequency	2.1916	-4.1140	-1.0039
	With modifications (b)	First natural frequency	1.5639	-1.6116	0.0043
	Without modifications (a)	Second natural frequency	1.9743	-5.5000	-1.6872
	With modifications (b)	Second natural frequency	2.4711	-2.5288	0.0166
5%	Without modifications (a)	First natural frequency	4.0516	-6.5084	-1.2515
	With modifications (b)	First natural frequency	2.5905	-2.7167	-0.0023
	Without modifications (a)	Second natural frequency	4.5330	-7.9145	-1.5097
	With modifications (b)	Second natural frequency	4.0647	-4.2317	0.0144

(where $a = ((f_H - f_F) / f_H) \times 100$) and between HOZT and mFSDT i.e. with modification, represented by b (where, $b = ((f_H - (f_F + e') / f_H) \times 100)$ for first and second natural frequencies. Note that an optimum sample size of 1024 (obtained based on Sobol sequence [46]) for GPR model formation, as required for the mFSDT framework, is decided based on a convergence study (refer to Table S1, Figure S1 of the supplementary material). Table 9 shows the percentage error values for first and second natural frequencies obtained with original FSDT with mFSDT for different values of degree of stochasticity (c) in the case of the laminated composite, while Table 10 shows the same for sandwich structures. Table 11 shows the percentage error values for different thickness values of laminates (t) in the case of the laminated composite, while Table 12 shows the same for sandwich structures. Table 13 shows the percentage error values for different E_1/ E_2 ratio values in the case of the laminated composite, while Table 14 shows the same study for sandwich structures. From all the above-mentioned tables, it is observed that the error values obtained after using mFSDT are significantly less compared to the error values obtained using original FSDT. Therefore, a generalized conclusion can be made that mFSDT provides more accurate results than the original FSDT.

Table 11: Percentage error for NF_1 and NF_2 obtained using original FSDT (without modification) and mFSDT (with modification) for different values of thickness of laminates (t) in case of laminated composite plates (for details about a and b refer to figure 4). Here the percentage error is obtained with respect to HOZT.

Thickness of laminates (t) in meter	Theory	Natural frequencies	Maximum percentage error (%)	Minimum percentage error (%)	Mean percentage error (%)
0.01m	Without modifications (a)	First natural frequency	3.8634	-0.7718	1.5749
	With modifications (b)	First natural frequency	1.2681	-1.2703	0.0311
	Without modifications (a)	Second natural frequency	6.8546	1.7074	4.2791
	With modifications (b)	Second natural frequency	1.7177	-1.6275	0.0309
0.011m	Without modifications (a)	First natural frequency	1.9339	-2.8599	-0.4357
	With modifications (b)	First natural frequency	1.2947	-1.2945	0.0322
	Without modifications (a)	Second natural frequency	4.1778	-1.1412	1.5157
	With modifications (b)	Second natural frequency	1.7670	-1.6747	0.0320
0.012m	Without modifications (a)	First natural frequency	-0.1184	-5.0791	-2.5735
	With modifications (b)	First natural frequency	1.3215	-1.3236	0.0323
	Without modifications (a)	Second natural frequency	1.3584	-4.1471	-1.3945

	With modifications (b)	Second natural frequency	1.8190	-1.7252	0.0327

Further, to reinforce the above conclusion, probability density function (pdf) plots (refer to figure 5-10) are presented showing percentage errors (%) for first and second natural frequency obtained with original FSDT, i.e., without modification, represented by a and with mFSDT, represented by $b$for different parameters in case of laminated composites and sandwich structure. Figure 5 shows the pdf plots showing percentage errors (%) for first and second natural frequencies obtained with original FSDT with mFSDT for different values of stochasticity (c) in case of the

Table 12: Percentage error for NF_1 and NF_2 obtained using original FSDT (without modification) and mFSDT (with modification) for different values of thickness of laminates (t) in case of sandwich plates (for details about a and b refer to figure 4). Here the percentage error is obtained with respect to HOZT.

Thickness of laminates (t) in meter	Theory	Natural frequencies	Maximum percentage error (%)	Minimum percentage error (%)	Mean percentage error (%)
0.01m	Without modifications (a)	First natural frequency	3.4370	-3.4090	-0.1467
	With modifications (b)	First natural frequency	1.6889	-1.5996	0.0123
	Without modifications (a)	Second natural frequency	10.6095	3.2946	7.1709
	With modifications (b)	Second natural frequency	2.3464	-2.3637	-0.0004
0.02m	Without modifications (a)	First natural frequency	2.1916	-4.1140	-1.0039
	With modifications (b)	First natural frequency	1.5639	-1.6116	0.0043
	Without modifications (a)	Second natural frequency	1.9743	-5.5000	-1.6872
	With modifications (b)	Second natural frequency	2.4711	-2.5288	0.0166
0.025m	Without modifications (a)	First natural frequency	-1.1151	-7.4832	-4.2062
	With modifications (b)	First natural frequency	1.6498	-1.6589	-0.0033
	Without modifications (a)	Second natural frequency	-2.5853	-10.4051	-6.5005
	With	Second natural	2.5974	-2.5309	0.0420

	modifications (b)	frequency			

laminated composite, while figure 6 shows the same for sandwich structures. Figure 7 shows percentage errors (%) for different thickness values of laminates (t) in the case of the laminated composite, while figure 8 shows the same for sandwich structures. Figure 9 shows the pdf plots showing percentage errors (%) for different E_1/ E_2 ratio values in the case of the laminated composite,

Table 13: Percentage error for NF_1 and NF_2 obtained using original FSDT (without modification) and mFSDT (with modification) for different values of E_1/ E_2 ratio in case of laminated composite plates (for details about a and b refer to figure 4). Here the percentage error is obtained with respect to HOZT.

E_1/ E_2	Theory	Natural frequencies	Maximum percentage error (%)	Minimum percentage error (%)	Mean percentage error (%)
3	Without modifications (a)	First natural frequency	1.7759	-3.1057	-0.6194
	With modifications (b)	First natural frequency	1.3709	-1.4083	0.0273
	Without modifications (a)	Second natural frequency	10.1218	5.0038	7.5636
	With modifications (b)	Second natural frequency	1.6728	-1.5477	0.0283
4	Without modifications (a)	First natural frequency	3.0484	-1.6825	0.7185
	With modifications (b)	First natural frequency	1.3087	-1.3248	0.0296
	Without modifications (a)	Second natural frequency	8.1891	3.0543	5.6196
	With modifications (b)	Second natural frequency	1.6995	-1.5900	0.0298
5	Without modifications (a)	First natural frequency	3.8634	-0.7718	1.5749
	With modifications (b)	First natural frequency	1.2681	-1.2703	0.0311
	Without modifications (a)	Second natural frequency	6.8546	1.7074	4.2791
	With modifications (b)	Second natural frequency	1.7177	-1.6275	0.0309

while figure 10 shows the same study for sandwich structures. From the above-mentioned figures, it is observed that the probability of occurrence of lesser absolute error is generally higher in case of mFSDT which corroborates its superiority in terms of prediction accuracy. However, note that the computational expenses of mFSDT remain almost the same as FSDT when multiple realizations are carried out for MCS. In fact, the computational expense of carrying out a few HOZT simulations for training the GPR becomes negligible compared to the case of carrying out MCS (~10^4 realizations) purely based on HOZT. Thus, the improved accuracy of mFSDT compared to FSDT does not come at the cost of more computational expenses in the present probabilistic analysis.

Table 14: Percentage error for NF_1 and NF_2 obtained using original FSDT (without modification) and mFSDT (with modification) for different values of E_1/E_2 ratio in case of sandwich plates (for details about *a* and *b* refer to figure 4). Here the percentage error is obtained with respect to HOZT.

E_1/E_2	Theory	Natural frequencies	Maximum percentage error (%)	Minimum percentage error (%)	Mean percentage error (%)
3	Without modifications (*a*)	First natural frequency	0.1195	-6.5113	-3.2792
	With modifications (*b*)	First natural frequency	1.6154	-1.6499	0.0049
	Without modifications (*a*)	Second natural frequency	3.5466	-3.8958	-0.1312
	With modifications (*b*)	Second natural frequency	2.4276	-2.4636	0.0096
4	Without modifications (*a*)	First natural frequency	1.9635	-4.3785	-1.2553
	With modifications (*b*)	First natural frequency	1.5672	-1.6138	0.0035
	Without modifications (*a*)	Second natural frequency	2.1633	-5.3066	-1.4990
	With modifications (*b*)	Second natural frequency	2.4583	-2.5211	0.0111
5	Without modifications (*a*)	First natural frequency	2.1916	-4.1140	-1.0039
	With modifications (*b*)	First natural frequency	1.5639	-1.6116	0.0043
	Without modifications (*a*)	Second natural frequency	1.9743	-5.5000	-1.6872
	With modifications (*b*)	Second natural frequency	2.4711	-2.5288	0.0166

c	NF_1	NF_2
1%	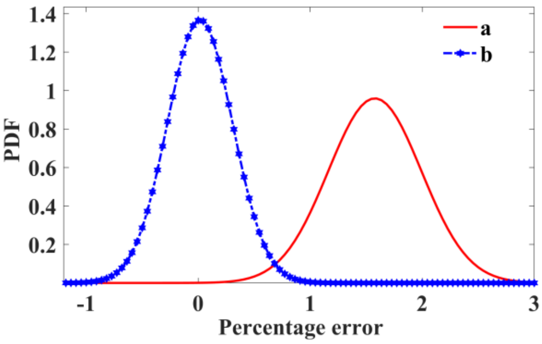 (a)	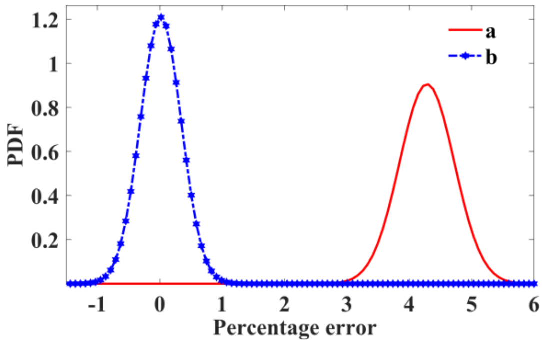 (b)
3%	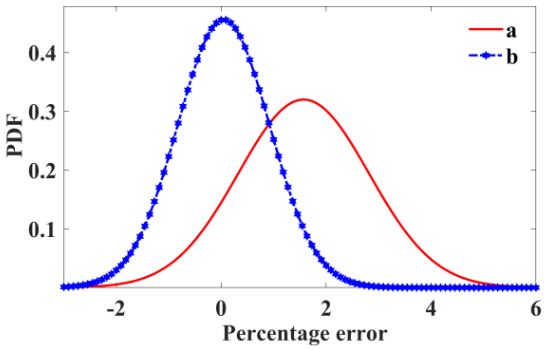 (c)	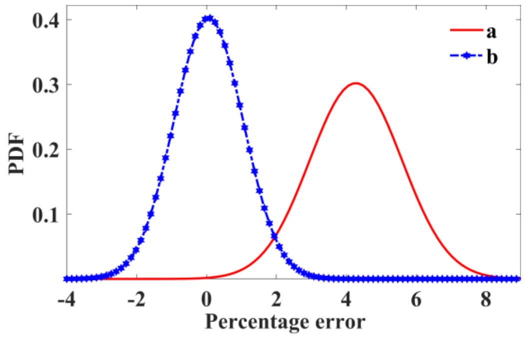 (d)
5%	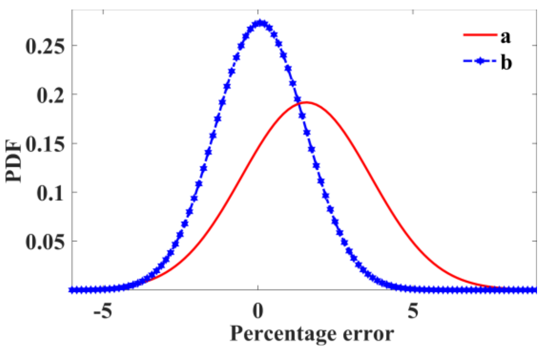 (e)	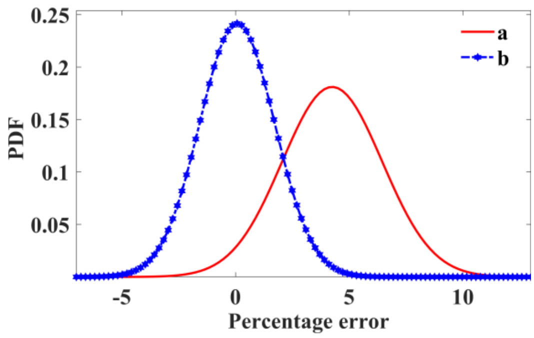 (f)

Fig. 5: PDF plots showing percentage errors (%) with respect to HOZT for (a, c, e) NF_1 and (b, d, e) NF_2 obtained using original FSDT and mFSDT for different values of stochasticity (c) in case of laminated composite plates. For details about a and b refer to figure 4.

<table>
<tr><th>c</th><th>NF_1</th><th>NF_2</th></tr>
<tr><td>1%</td><td>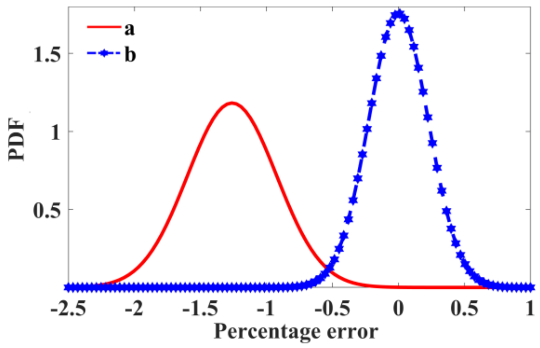

(a)</td><td>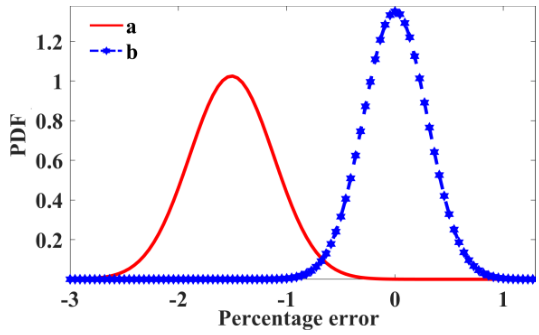

(b)</td></tr>
<tr><td>3%</td><td>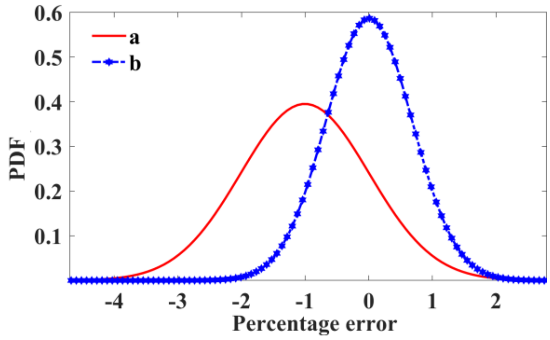

(c)</td><td>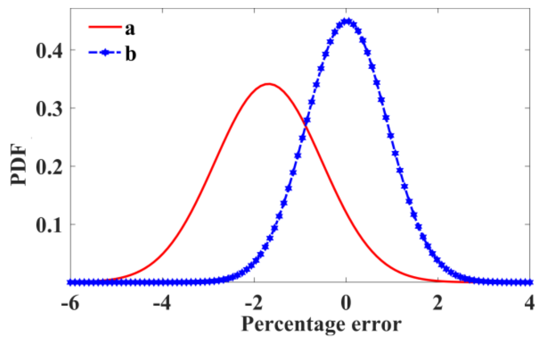

(d)</td></tr>
<tr><td>5%</td><td>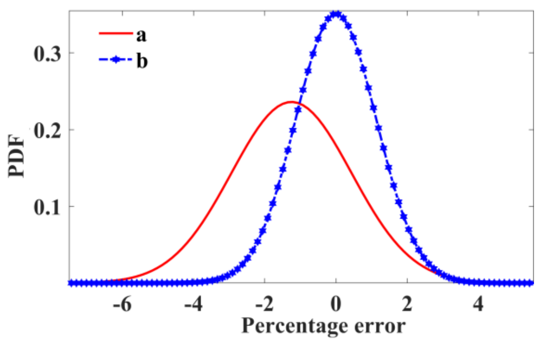

(e)</td><td>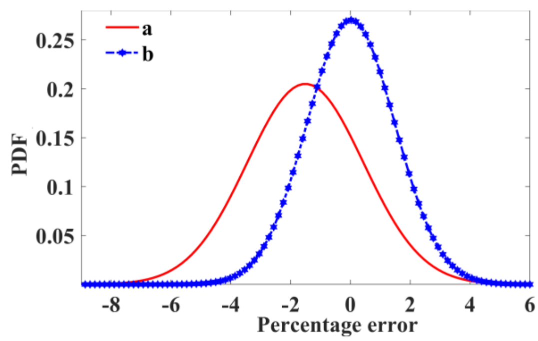

(f)</td></tr>
</table>

Fig. 6: PDF plots showing percentage errors (%) with respect to HOZT for (a, c, e) NF_1 and (b, d, e) NF_2 obtained using original FSDT and mFSDT for different values of stochasticity (c) in case of sandwich plates. For details about a and b refer to figure 4.

t	NF_1	NF_2
0.01m	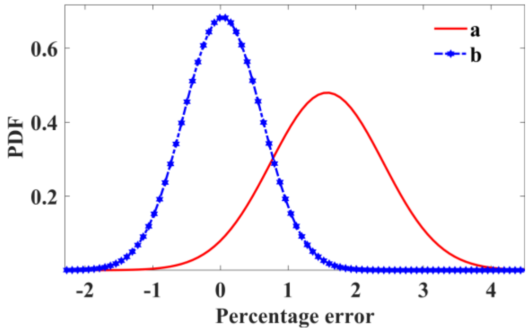 (a)	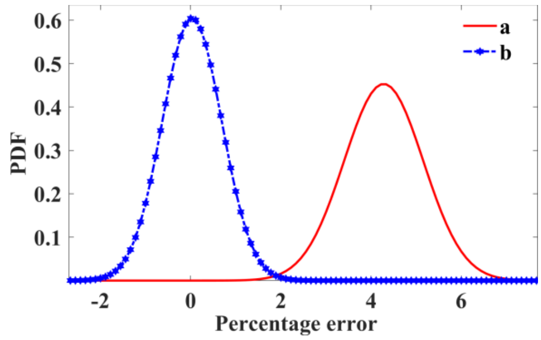 (b)
0.011m	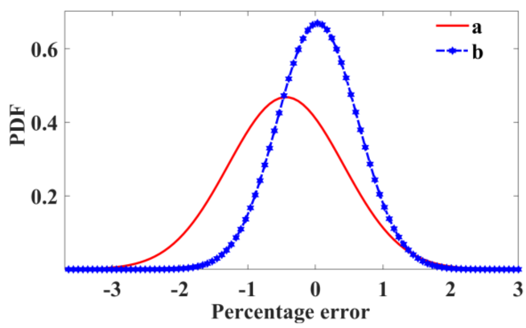 (c)	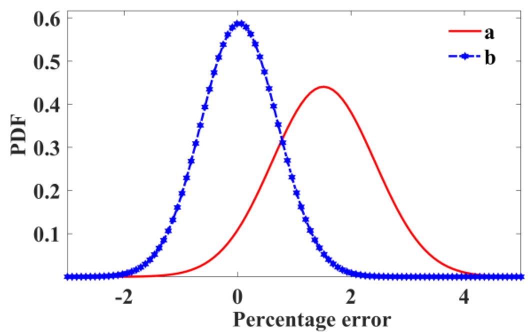 (d)
0.012m	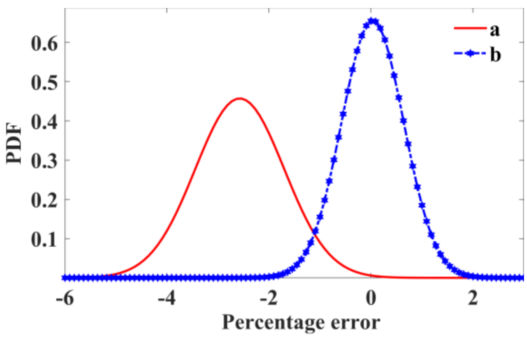 (e)	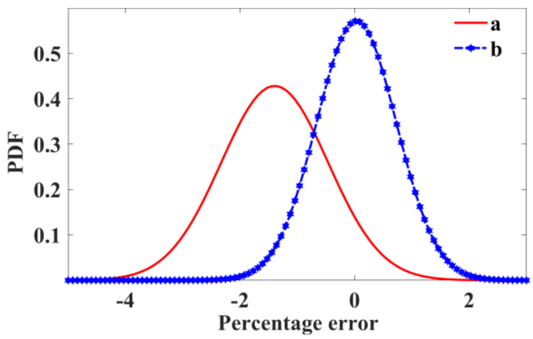 (f)

Fig. 7: PDF plots showing percentage errors (%) with respect to HOZT for (a, c, e) NF_1 and (b, d, e) NF_2 obtained using original FSDT and mFSDT for different values of thickness of laminates (t) in case of laminated composite plates. For details about a and b refer to figure 4.

t	NF_1	NF_2
0.01m	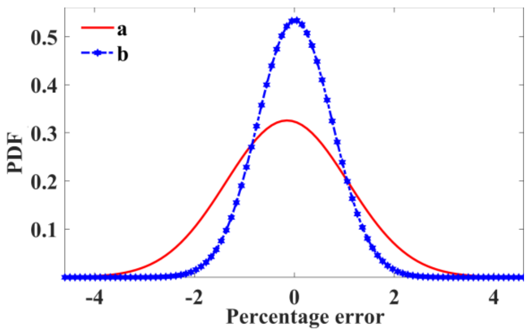 (a)	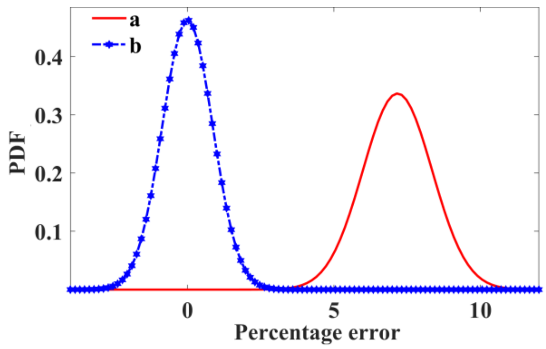 (b)
0.02m	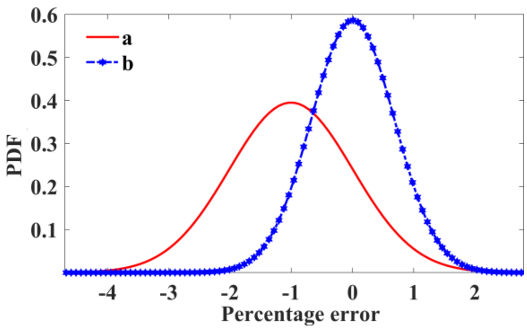 (c)	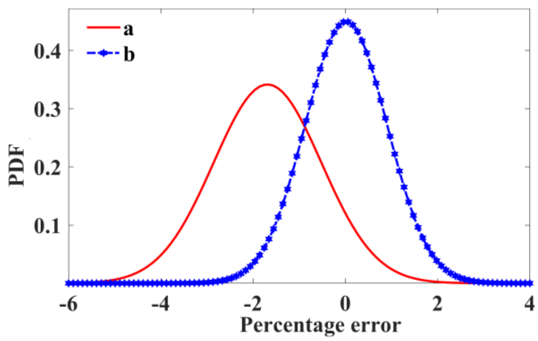 (d)
0.025m	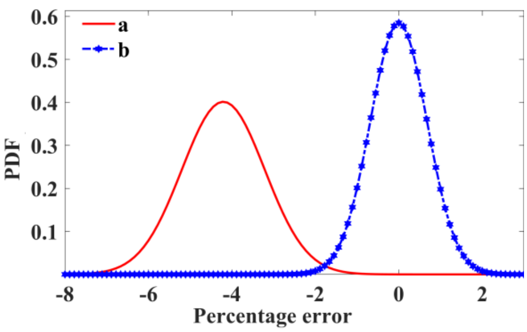 (e)	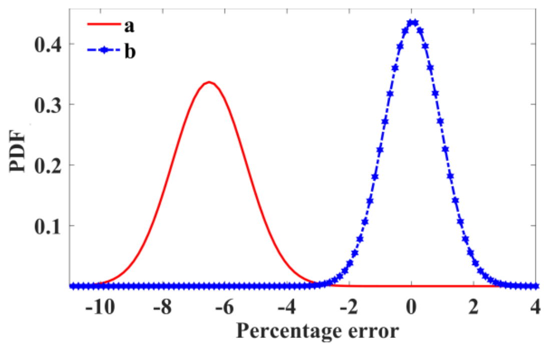 (f)

Fig. 8: PDF plots showing percentage errors (%) with respect to HOZT for (a, c, e) NF_1 and (b, d, e) NF_2 obtained using original FSDT and mFSDT for different values of thickness of laminates (t) in case of sandwich plates. For details about a and b refer to figure 4.

E_1/E_2	NF_1	NF_2
3	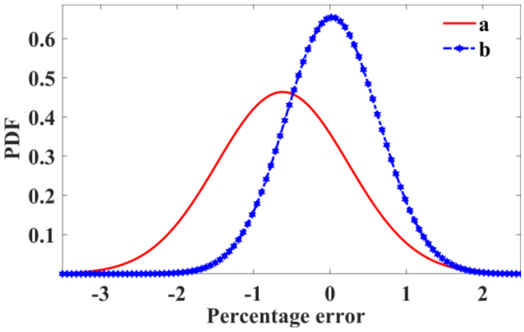 (a)	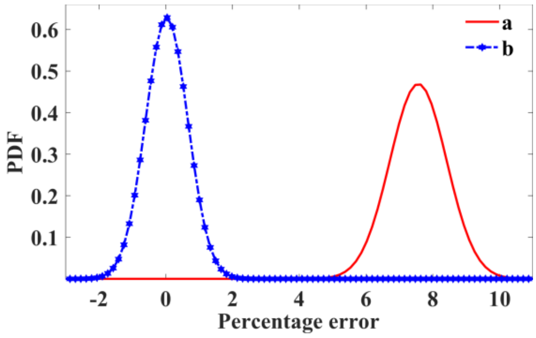 (b)
4	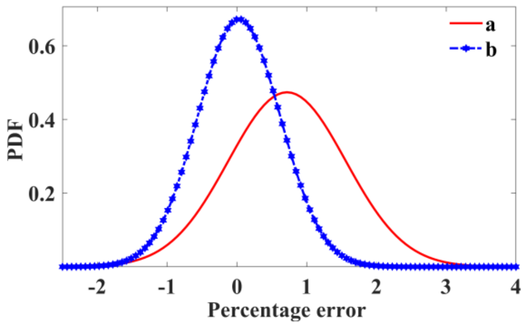 (c)	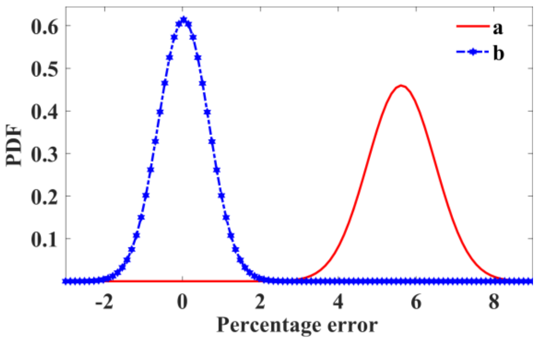 (d)
5	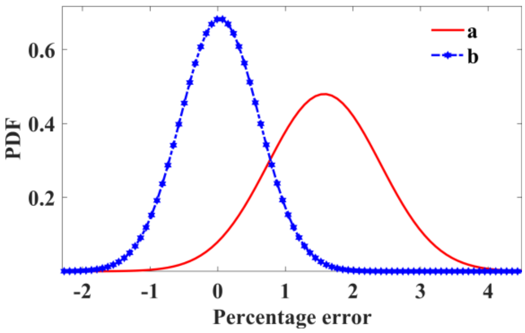 (e)	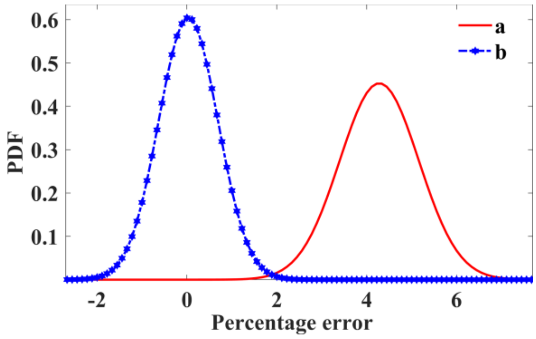 (f)

Fig. 9: PDF plots showing percentage errors (%) with respect to HOZT for (a, c, e) NF_1 and (b, d, e) NF_2 obtained using original FSDT and mFSDT for different values of E_1/E_2 ratio in case of laminated composite plates. For details about *a* and *b* refer to figure 4.

E_1/E_2	NF_1	NF_2
3	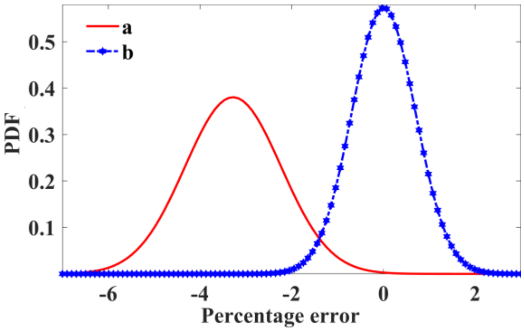 (a)	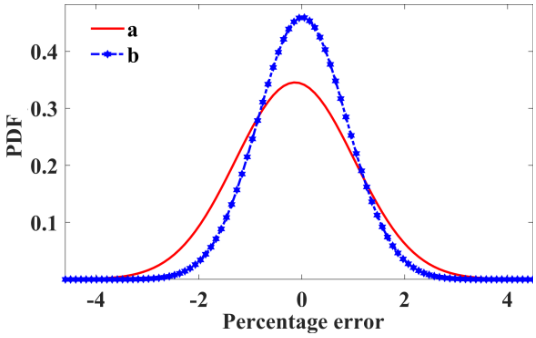 (b)
4	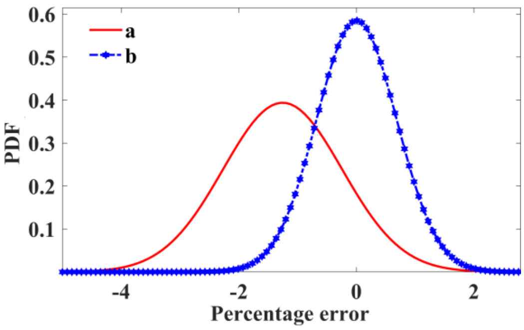 (c)	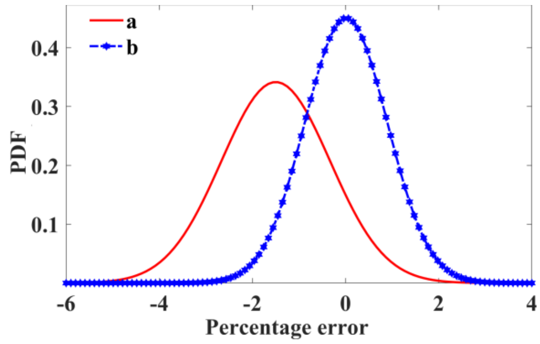 (d)
5	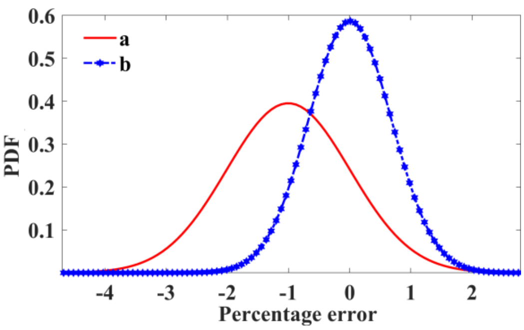 (e)	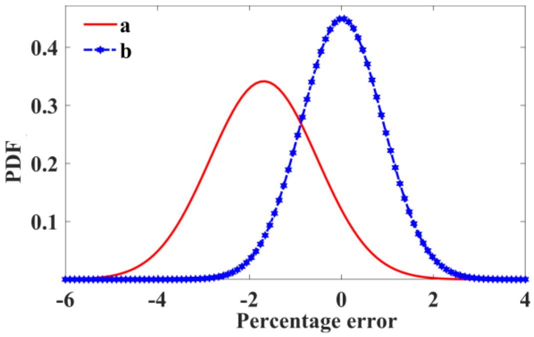 (f)

Fig. 10: PDF plots showing percentage errors (%) with respect to HOZT for (a, c, e) NF_1 and (b, d, e) NF_2 obtained using original FSDT and mFSDT for different values of E_1/E_2 ratio in case of sandwich plates. For details about *a* and *b* refer to figure 4.

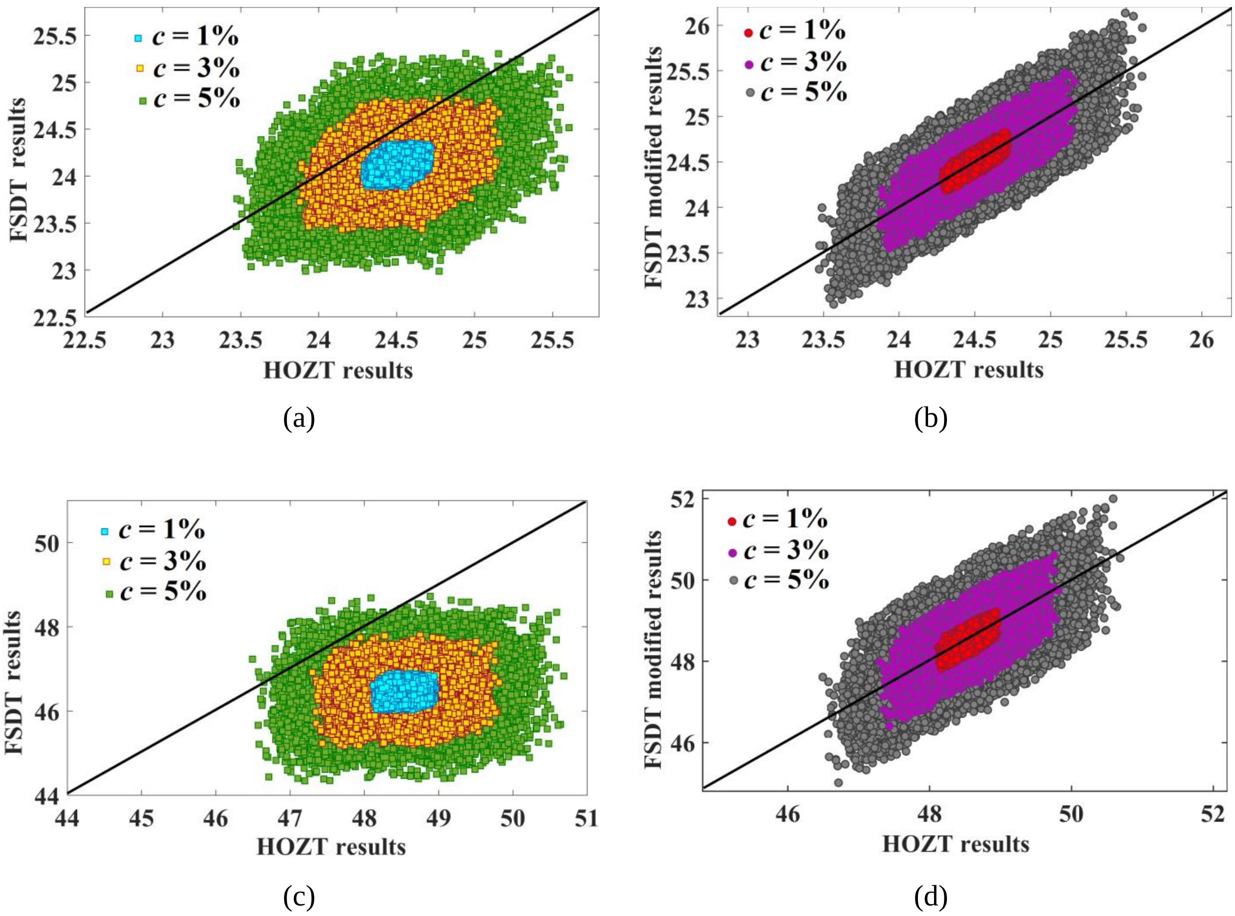

Fig. 11: Scatter plots for (a, b) NF_1 and (c, d) NF_2 obtained between the predictions based on HOZT and original FSDT or mFSDT (i.e. FSDT modified results based on GPR) considering different values of degree of stochasticity (c) in the case of laminated composite plates. Note that the prediction capacity of the quantity(s) plotted on the y-axis is considered to be more accurate with respect to the quantity plotted on x-axis when the scattered points lie close to the diagonal line.

Scatter plots can provide a direct sample to sample visual representation of the prediction ability of mFSDT compared to HOZT. Thus, scatter plots are presented for validating the results obtained using mFSDT with respect to HOZT (refer to figures 11-16). For a better understanding of the comparative accuracy of FSDT and mFSDT with respect to HOZT, both the results are shown for various cases. Figure 11 presents the scatter plots for first and second natural frequencies obtained with original FSDT, mFSDT, and HOZT for different values of stochasticity (c) in the case of the laminated composite, while figure 12 shows the same for sandwich structures. Figure 13 shows the scatter plot for different thickness values of laminates (t) in the case of the laminated composite, while figure 14 shows the same for sandwich structures. Figure 15 shows a scatter plot for different E_1/E_2 ratio values in the case of the laminated composite, while figure 16 shows the same study for

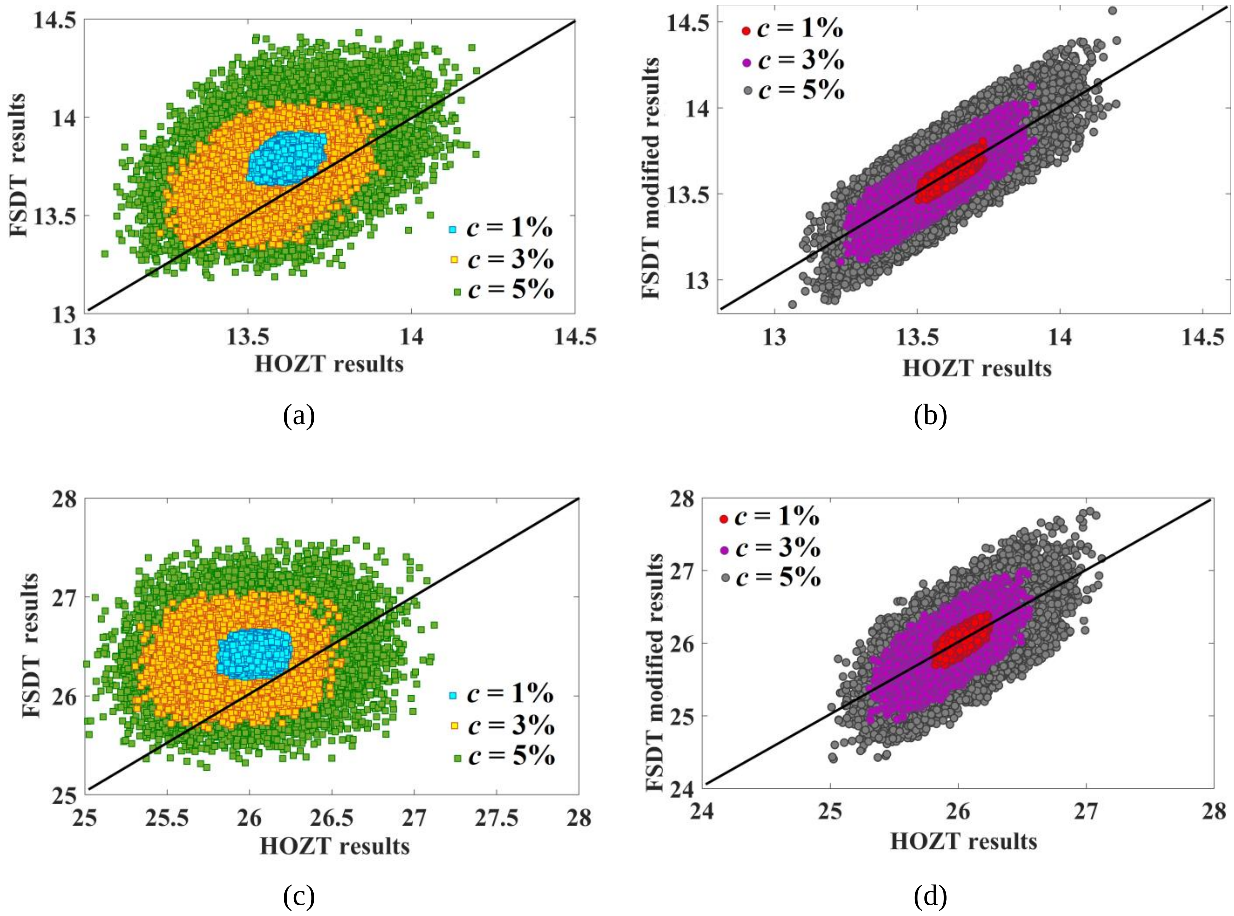

Fig. 12: Scatter plots for (a, b) NF_1 and (c, d) NF_2 obtained between the predictions based on HOZT and original FSDT or mFSDT (i.e. FSDT modified results based on GPR) considering different values of degree of stochasticity (c) in the case of sandwich plates. Note that the prediction capacity of the quantity(s) plotted on the y-axis is considered to be more accurate with respect to the quantity plotted on x-axis when the scattered points lie close to the diagonal line.

sandwich structures. From all the above-mentioned figures, a general observation can be made that the results obtained from mFSDT show less deviation with respect to the results of HOZT. This indicates the excellent prediction accuracy of mFSDT compared to FSDT.

After confirming the accuracy and prediction capability of mFSDT results, the study is further extended here to investigatethe complete probabilistic descriptions of first and second natural frequencies considering different cases of uncertainties using mFSDT. It may be noted that a stochastically varying framework of depth-wise material properties (i.e. layer-wise random variable approach) is considered for modeling the uncertainty for both laminated composite structure and sandwich structure. Figures 17-22 show probability density function (pdf) plots depicting the outcome of various critical parameters on the probabilistic natural frequency of laminated composite

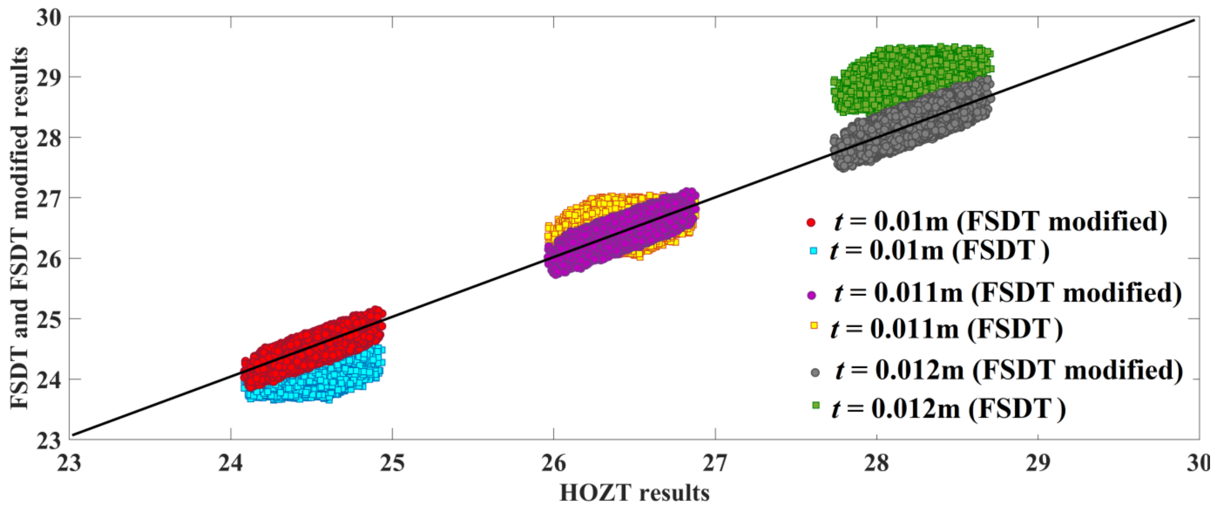

(a)

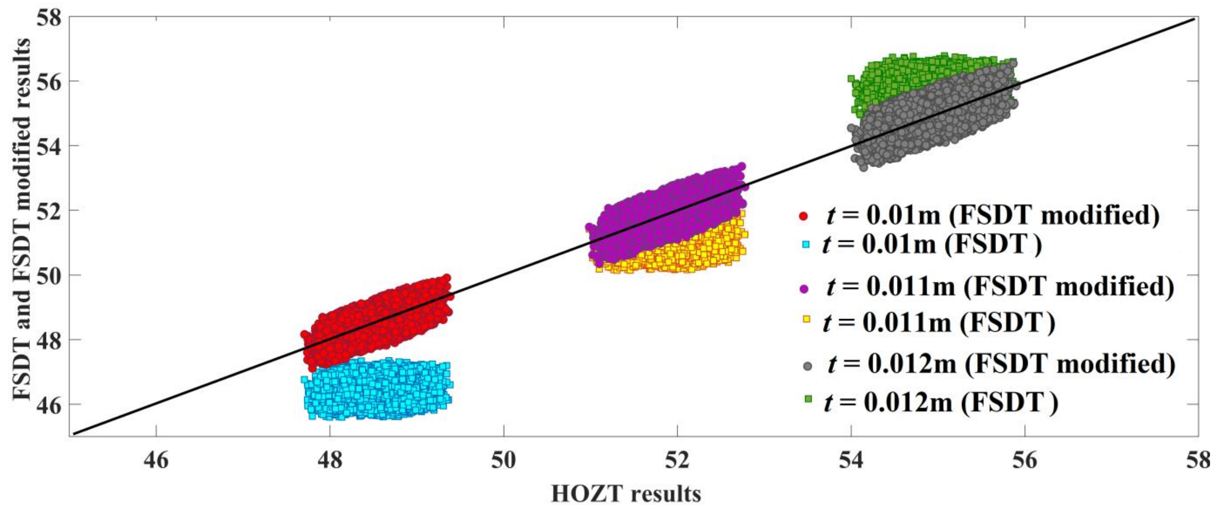

(b)

Fig. 13: Scatter plots for (a, b) NF_1 and (c, d) NF_2 obtained between the predictions based on HOZT and original FSDT or mFSDT (i.e. FSDT modified results based on GPR) considering different values of thickness of laminates (t) in the case of laminated composite plates. Note that the prediction capacity of the quantity(s) plotted on the y-axis is considered to be more accurate with respect to the quantity plotted on x-axis when the scattered points lie close to the diagonal line.

plate and on the sandwich structure. Figure 17 shows the pdf plots for first and second natural frequencies obtained by applying mFSDT for different values of degree of stochasticity (c) in the case of the laminated composite plate, while figure 18 shows the same for sandwich structures. It is witnessed that on incrementing stochasticity value, the response bound for the natural frequencies for both laminated composite and sandwich structure also increases. In contrast, no or marginal effect on their mean values is noticed.

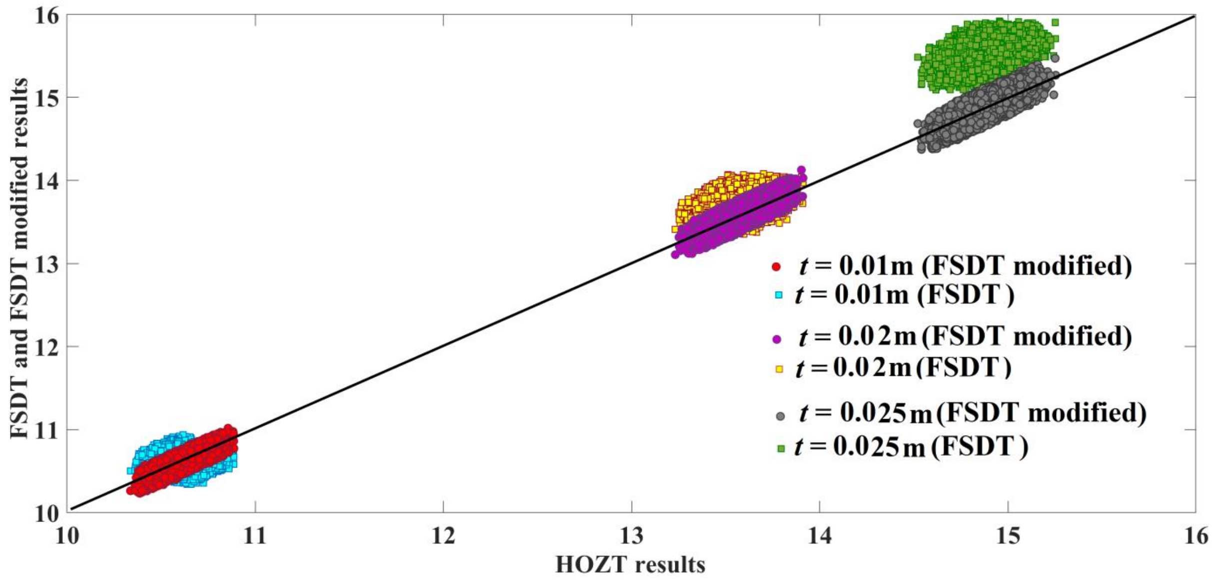

(a)

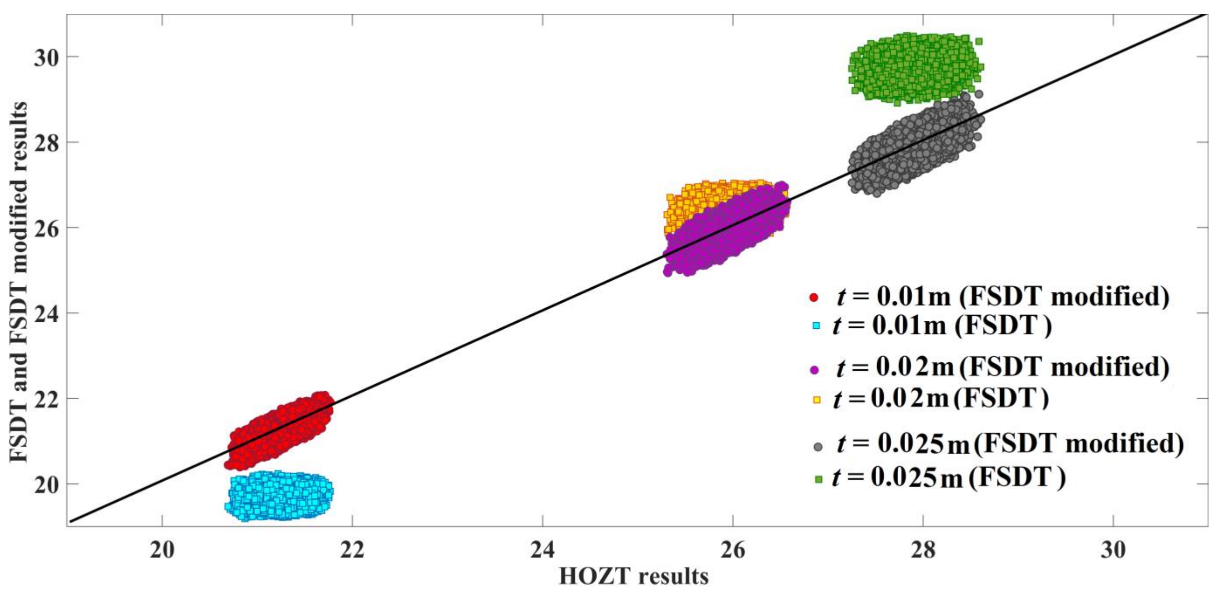

(b)

Fig. 14: Scatter plots for (a, b) NF_1 and (c, d) NF_2 obtained between the predictions based on HOZT and original FSDT or mFSDT (i.e. FSDT modified results based on GPR) considering different values of thickness of laminates (t) in the case of sandwich plates. Note that the prediction capacity of the quantity(s) plotted on the y-axis is considered to be more accurate with respect to the quantity plotted on x-axis when the scattered points lie close to the diagonal line.

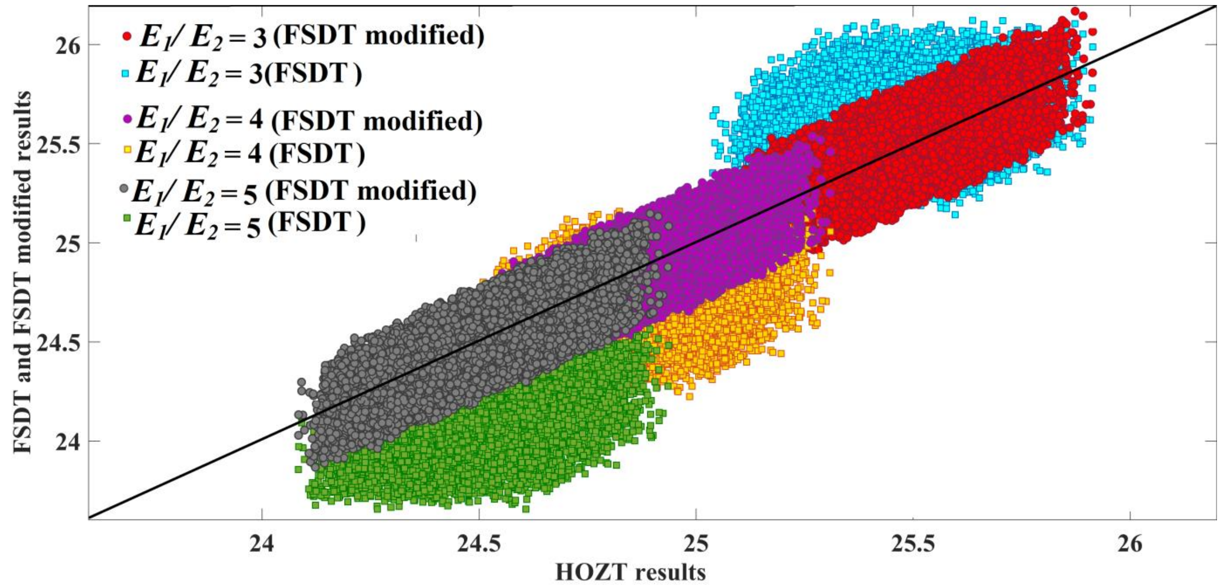

(a)

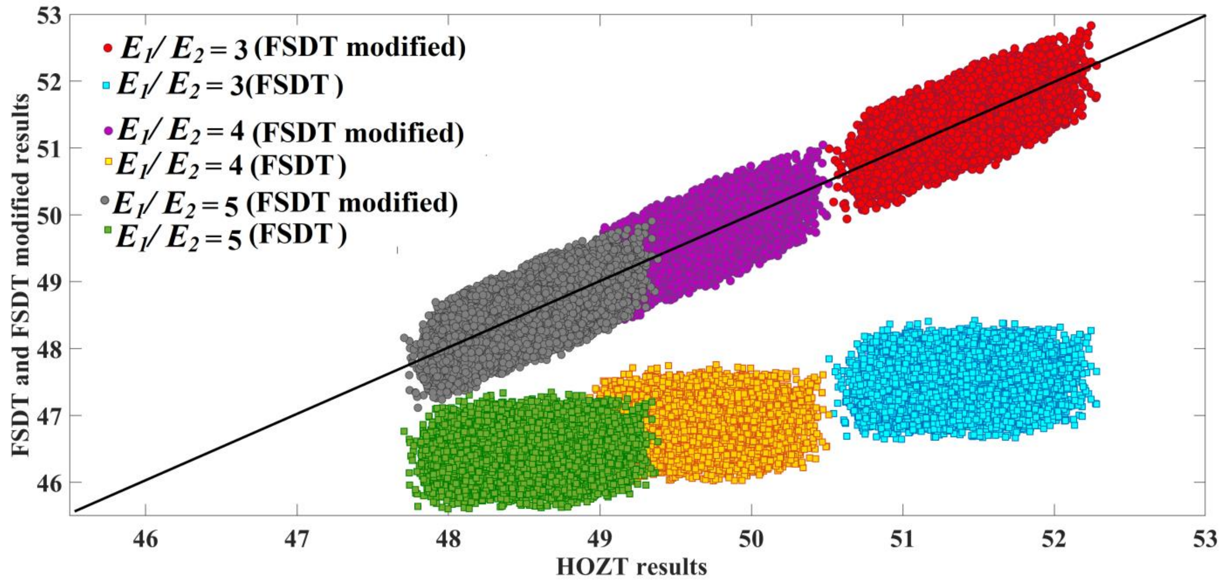

(b)

Fig. 15: Scatter plots for (a, b) NF_1 and (c, d) NF_2 obtained between the predictions based on HOZT and original FSDT or mFSDT (i.e. FSDT modified results based on GPR) considering different values of E_1/E_2 ratio in the case of laminated composite plates. Note that the prediction capacity of the quantity(s) plotted on the y-axis is considered to be more accurate with respect to the quantity plotted on x-axis when the scattered points lie close to the diagonal line.

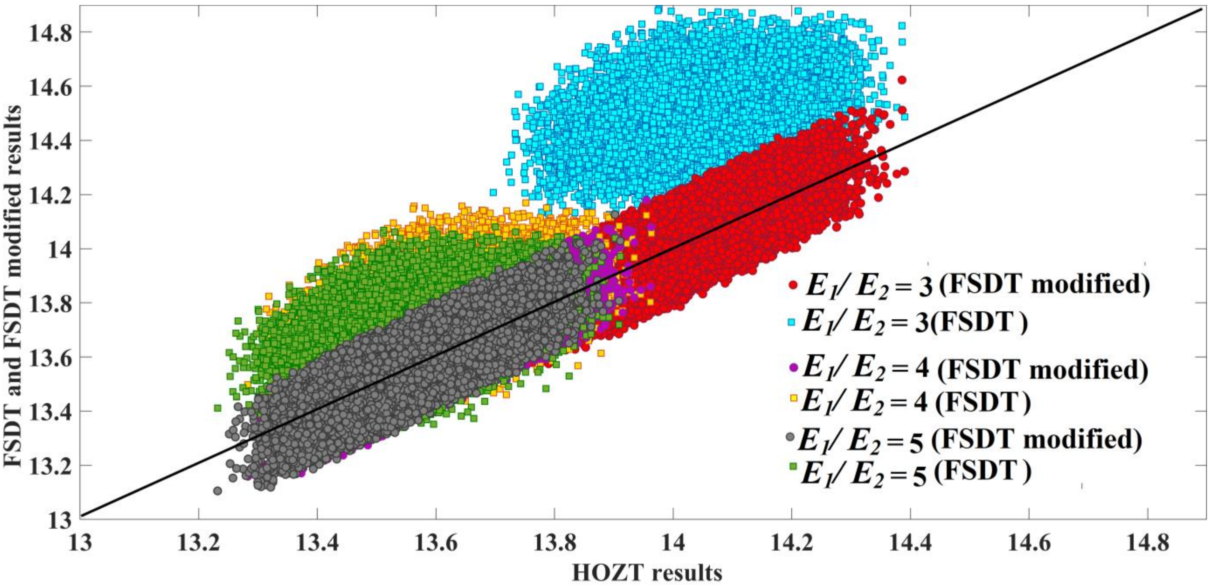

(a)

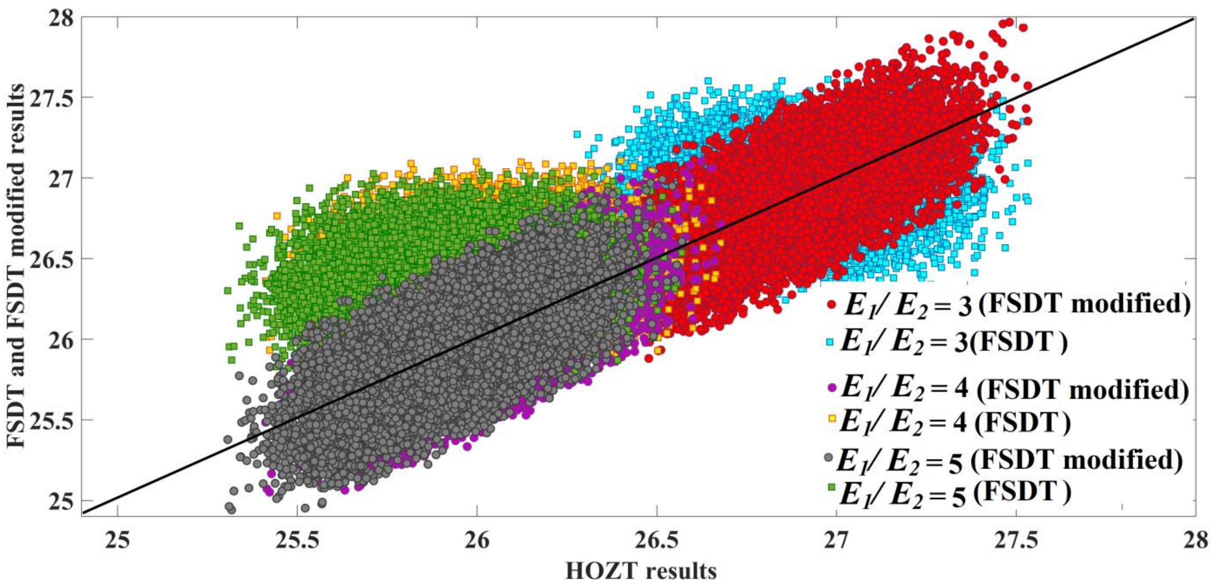

(b)

Fig. 16: Scatter plots for (a, b) NF_1 and (c, d) NF_2 obtained between the predictions based on HOZT and original FSDT or mFSDT (i.e. FSDT modified results based on GPR) considering different values of E_1/E_2 ratio in the case of sandwich plates. Note that the prediction capacity of the quantity(s) plotted on the y-axis is considered to be more accurate with respect to the quantity plotted on x-axis when the scattered points lie close to the diagonal line.

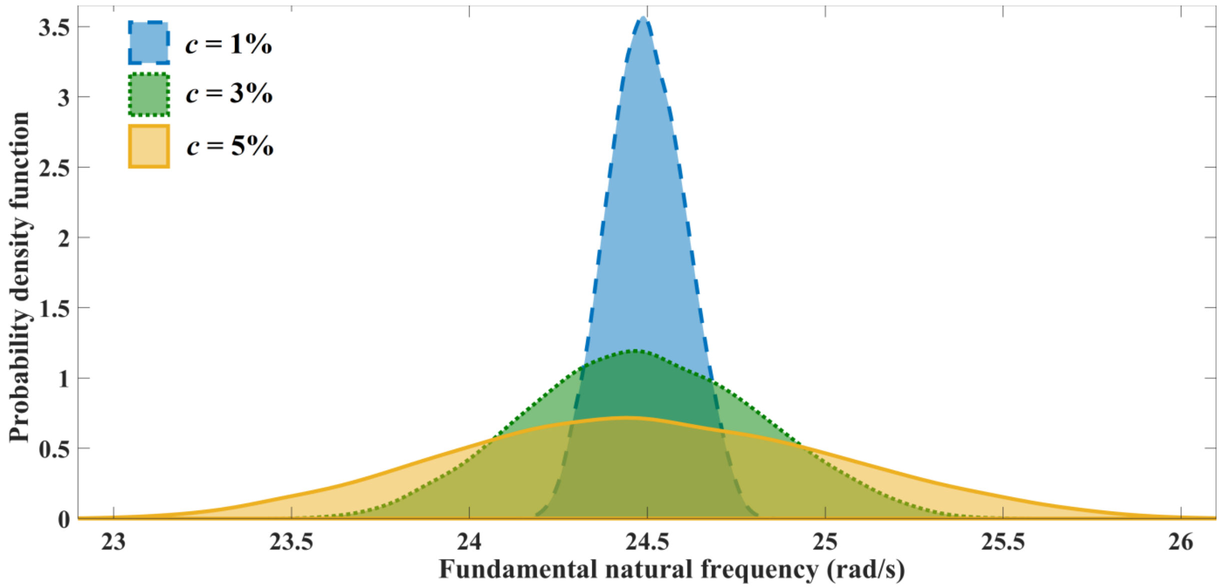

(a)

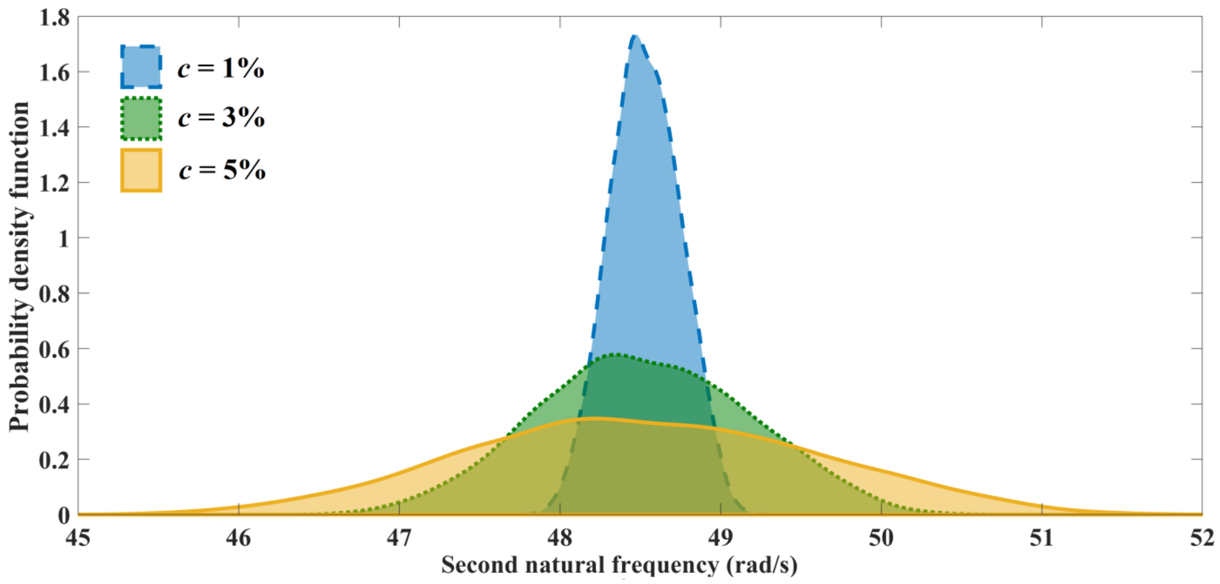

(b)

Fig. 17: PDF plots for (a) NF_1 and (b) NF_2obtained using mFSDT for different values of degree of stochasticity (c) in case of laminated composite plates. The layer-wise structural configurations and geometric details, deterministic material properties and the stochastic representations are depicted in section 2.6 and the introductory paragraphs of section 3. The PDF plots show here that the mean values remain almost unaltered with different degrees of stochasticity (c), while the stochastic response bounds increase with the increase in c.

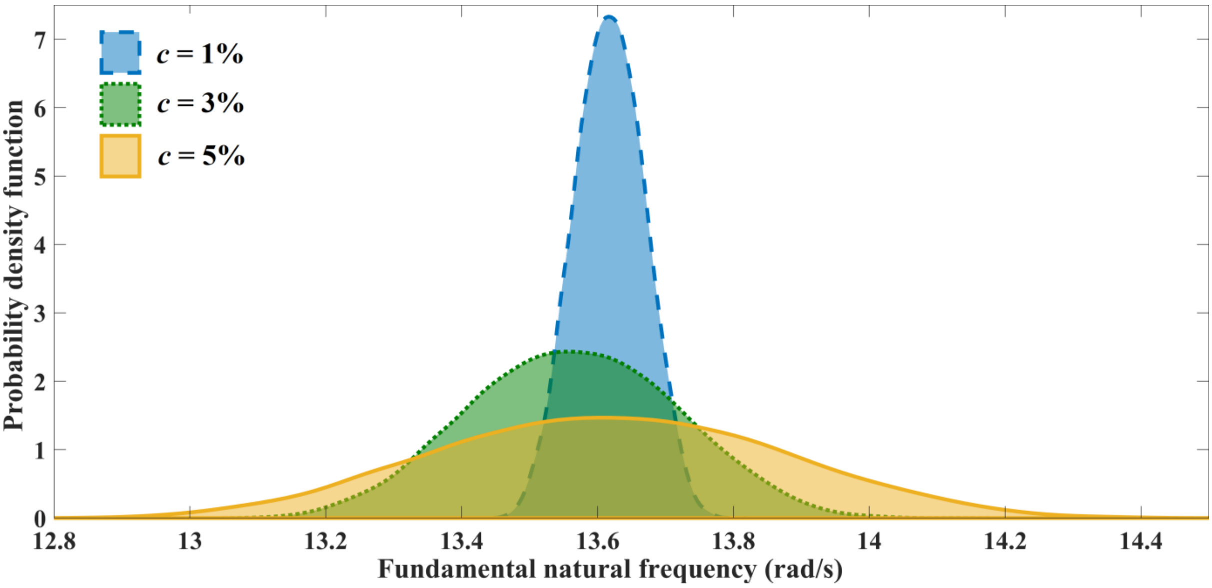

(a)

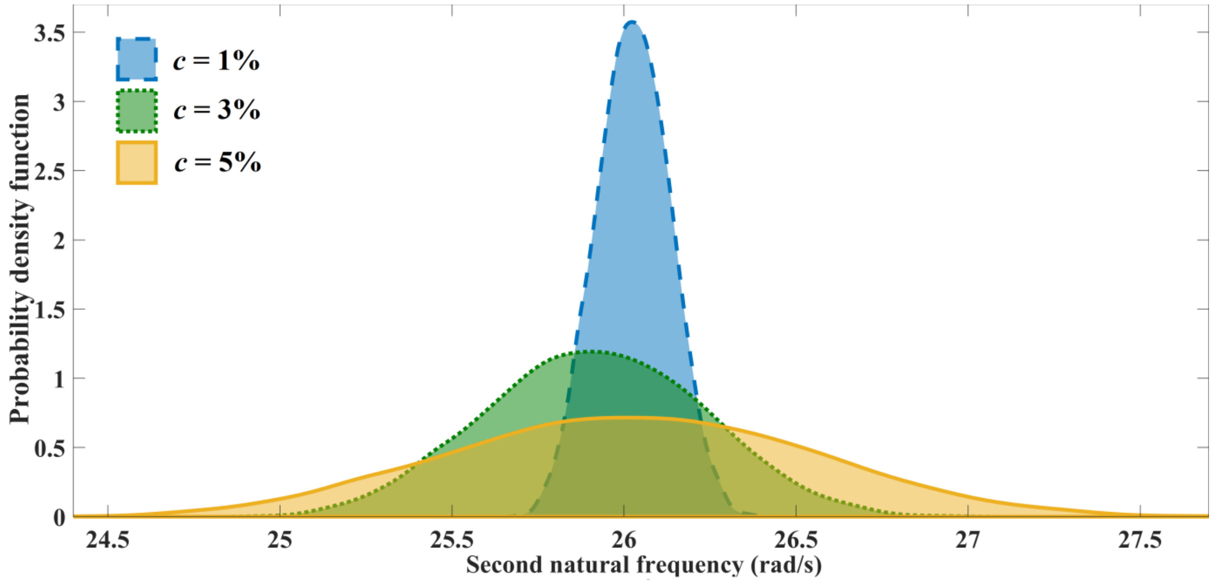

(b)

Fig. 18: PDF plots for (a) NF_1 and (b) NF_2obtained using mFSDT for different values of degree of stochasticity (c) in case of sandwich plates. The layer-wise structural configurations and geometric details, deterministic material properties and the stochastic representations are depicted in section 2.6 and the introductory paragraphs of section 3. The PDF plots show here that the mean values remain almost unaltered with different degrees of stochasticity (c), while the stochastic response bounds increase with the increase in c.

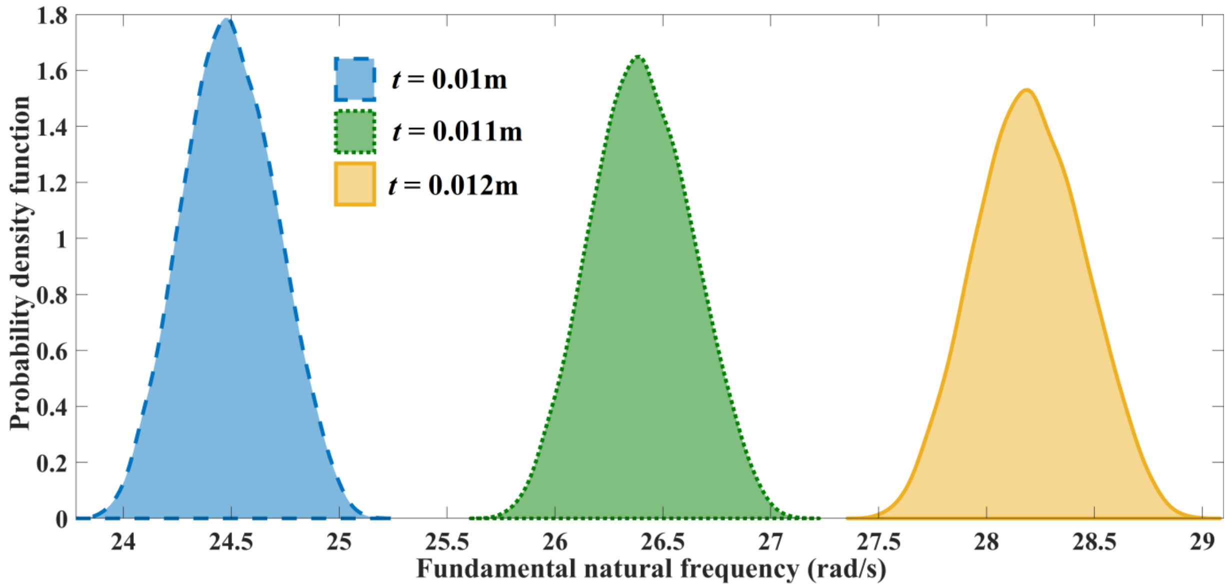

(a)

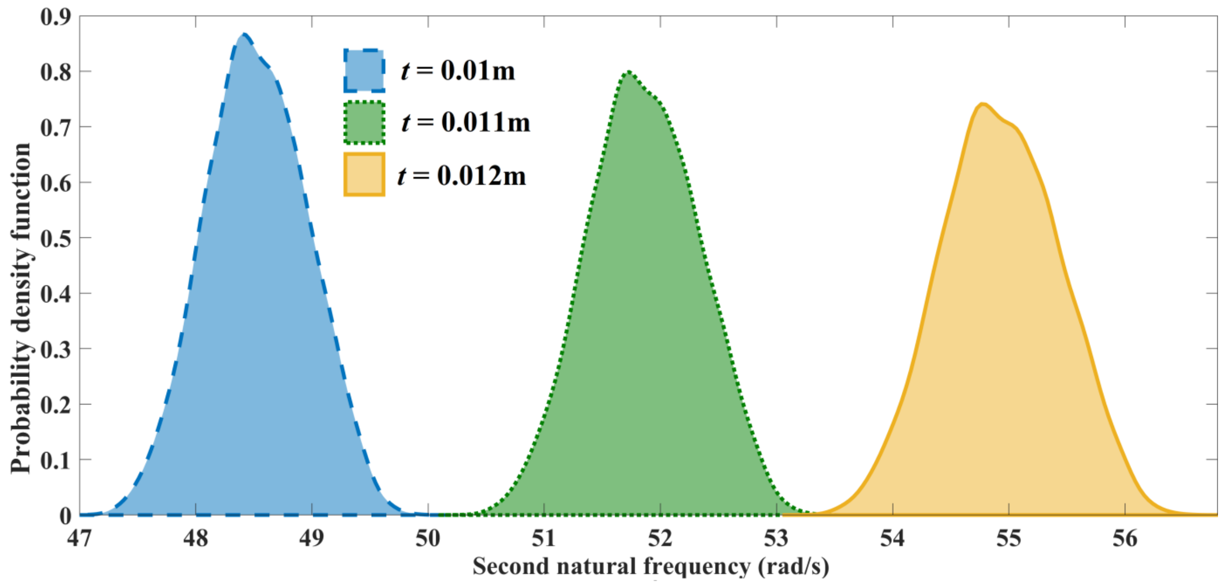

(b)

Fig. 19: PDF plots for (a) NF_1 and (b) NF_2obtained using mFSDT for different values of thickness of laminates (t) in case of laminated composite plates. The layer-wise structural configurations and geometric details, deterministic material properties and the stochastic representations are depicted in section 2.6 and the introductory paragraphs of section 3. The PDF plots show here that the mean values follow the deterministic physics-based trends with respect to thickness, while the stochastic response bounds show a coupled effect of uncertainty with the material parameters.

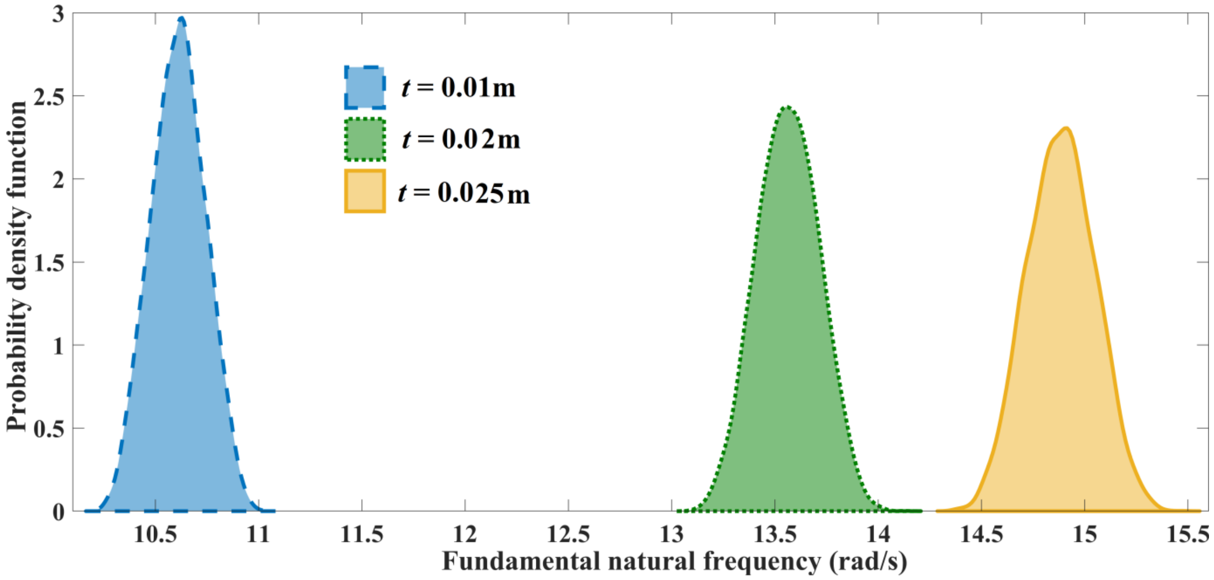

(a)

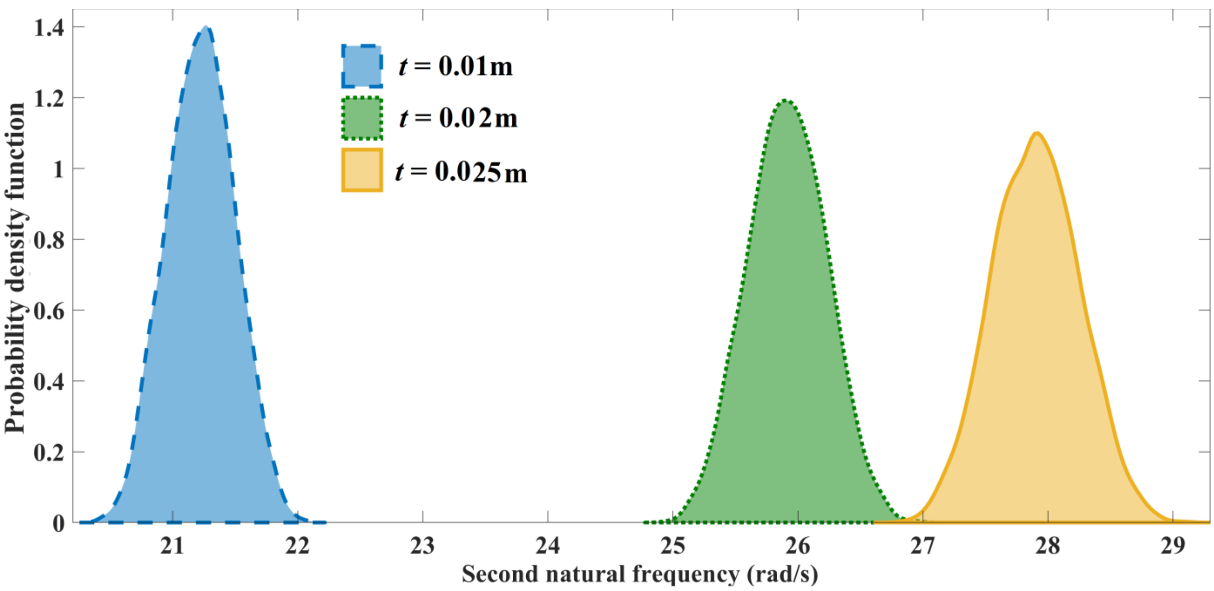

(b)

Fig. 20: PDF plots for (a) NF_1 and (b) NF_2obtained using mFSDT for different values of thickness of laminates (t) in case of sandwich plates. The layer-wise structural configurations and geometric details, deterministic material properties and the stochastic representations are depicted in section 2.6 and the introductory paragraphs of section 3. The PDF plots show here that the mean values follow the deterministic physics-based trends with respect to thickness, while the stochastic response bounds show a coupled effect of uncertainty with the material parameters.

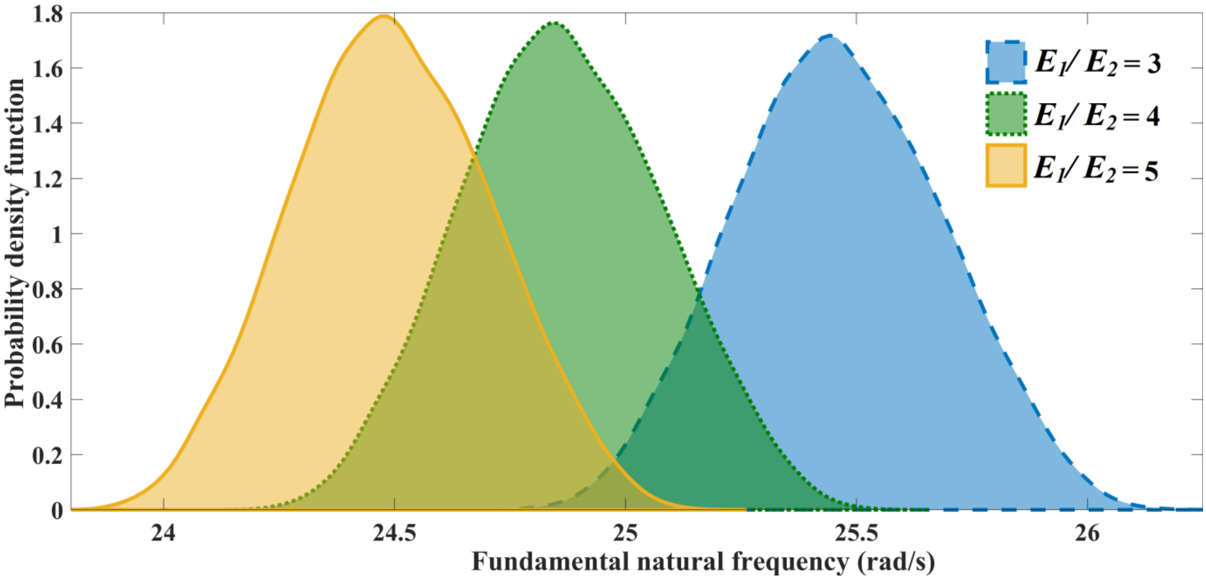

(a)

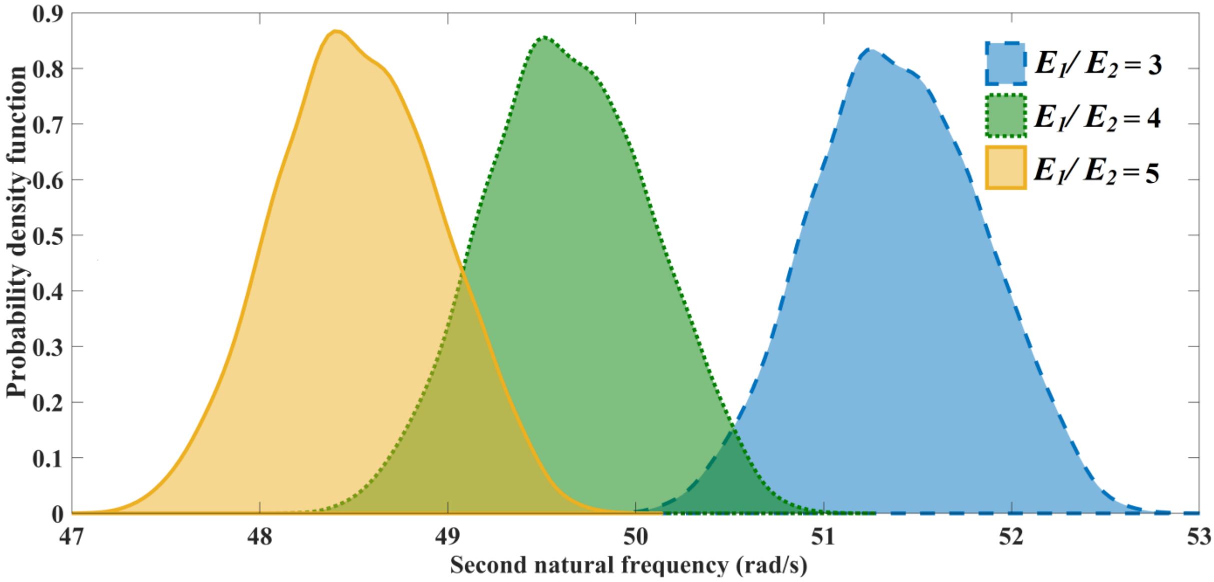

(b)

Fig. 21: PDF plots for (a) NF_1 and (b) NF_2obtained using mFSDT for different values of E_1/E_2 ratio in case of laminated composite plates. The layer-wise structural configurations and geometric details, deterministic material properties and the stochastic representations are depicted in section 2.6 and the introductory paragraphs of section 3. The PDF plots show here that the mean values follow the deterministic physics-based trends with respect to degree of orthotropy, while the stochastic response bounds show a coupled effect of uncertainty with the material parameters.

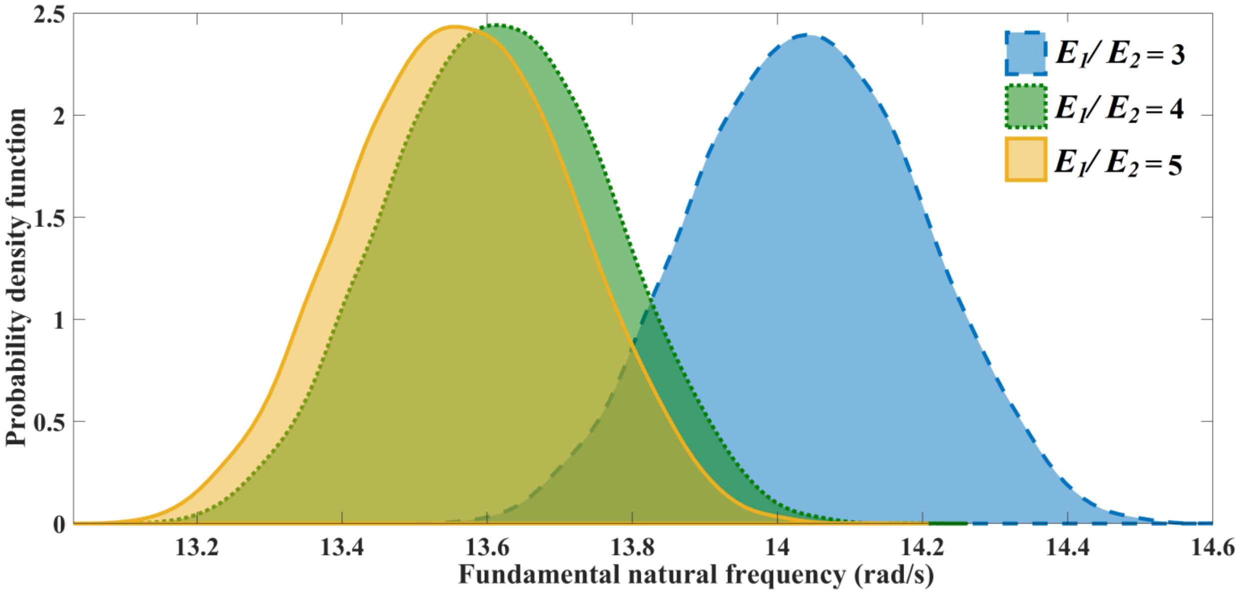

(a)

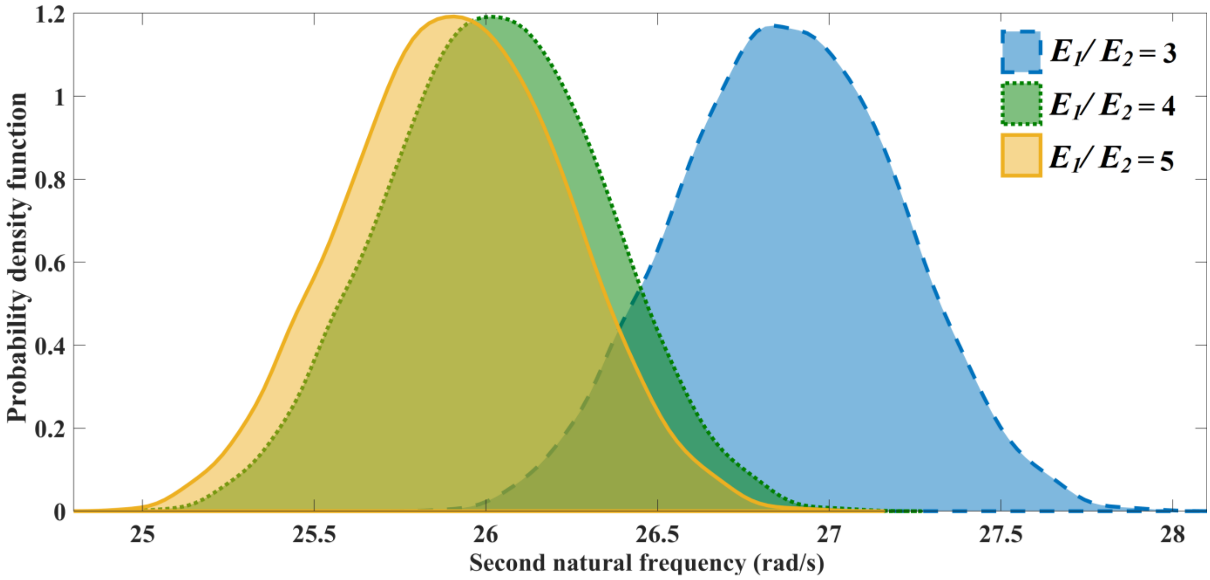

(b)

Fig. 22: PDF plots for (a) NF_1 and (b) NF_2 obtained using mFSDT for different values of E_1/E_2 ratio in case of sandwich plates. The layer-wise structural configurations and geometric details, deterministic material properties and the stochastic representations are depicted in section 2.6 and the introductory paragraphs of section 3. The PDF plots show here that the mean values follow the deterministic physics-based trends with respect to degree of orthotropy, while the stochastic response bounds show a coupled effect of uncertainty with the material parameters.

Figure 19 shows the pdf plots for different thickness values of laminates (t) in the case of the laminated composite plate, while figure 20 shows the same for sandwich structures. In both cases, it is observed that the standard deviation and the mean values of natural frequencies increase on incrementing the thickness value. Figure 21 shows a pdf plot for different E_1/E_2 ratio values in the case of the laminated composite, while figure 22 shows the same study for sandwich structures. It is noticed that on incrementing the values of E_1/E_2 ratio, the natural frequency value decreases in both cases. It can be noted here that while the nature and stochastic bounds of these probabilistic plots depend on the coupled stochastic effect of different source uncertainties, the trends of the mean values follow the basic deterministic results concerning the physics involved in the critical input parameters of interest. The current approach of carrying out the MCS based on mFSDT for obtaining these probabilistic descriptions reduces the computational expenses significantly compared to HOZT based analyses without compromising the accuracy. Since a sample size of 1024 is used for the GPR model formation, which is subsequently used in the mFSDT formation, the computational efficiency of more than 29 times can be achieved for each of the cases of probabilistic analysis presented in this section considering different degrees of stochasticity.

4. Conclusions and perspective

A novel concept of modified first-order shear deformation theory (mFSDT) is proposed in this article for achieving a similar level of accuracy as the higher-order theories like HOZT (higher-order zigzag theory) in large scale simulations involving thousands of realizations while keeping the computational expenses similar to lower-order theories. This is achieved by developing a computational bridging between first-order shear deformation theory (FSDT) and HOZT through Gaussian process-based machine learning.In general, FSDT is less accurate compared to higher-order theories like HOZT. For large-scale simulation-based analyses like uncertainty quantification and optimization (where the number of realizations required can be as high as ~10^4) using FSDT, such errors propagate and accumulate over multiple realizations, leading to significantly erroneous results. Consideration of higher-order theories results in significantly increased computational expenses, even though these theories are more accurate. Note that the computational expense of carrying out ~10^4 simulations (for uncertainty quantification, optimization, or other large-scale simulation-based analyses) would be exorbitant when each of the simulations is expensive.

To address the issues of accuracy and computational efficiency simultaneously, we have exploited machine learning to develop the theory of mFSDT, based on which extensive deterministic results and Monte Carlo simulation-assisted probabilistic results are presented here for the free vibration analysis of laminate composite plates and sandwich structures. Before investigating the probabilistic descriptions of natural frequencies critically, extensive validation studies are presented concerning the predictions of FSDT, HOZT and mFSDT. The performance of mFSDT essentially depends on the accuracy of GPR model, which is ensured in terms of scatter plots, probabilistic error profiles and statistical moments. Since a sample size of 1024 is used here for the GPR model formation, which is subsequently used in the mFSDT formation, a computational efficiency of more than 29 times can be achieved for each of the cases of probabilistic analysis presented in this paper covering different degrees of stochasticity.

Based on mFSDT, the complete probabilistic descriptions of natural frequencies are investigated for composite laminates and sandwich structures with composite face sheets, wherein the effect of layer-wise thickness and degree of orthotropy are presented by considering the compound critical influence of material uncertainty. The numerical results reveal that the effect of uncertainty gets pronounced significantly while propagating from the compound source level to the global free vibration characteristics. Such outcomes based on quantitative data essentially bring us to the realization that the inclusion of uncertainty is of utmost importance in developing a reliable and practically relevant analysis and design framework for composite structures which have a compound high-dimensional space of source uncertainties due to multiple constituent components and orthotropic material properties. The proposed algorithm of bridging different laminate theories is generic in nature and it can be utilized further for connecting other deformation theories to develop a unified framework, leading to a range of large-scale data-driven static and dynamic analyses of complex structural forms for accurate, yet computationally efficient predictions.

Acknowledgments

Vaishali acknowledges the MoE, Govt. of India, for the support provided during this work. TM acknowledges the initiation grant from IIT Kanpur.

Data availability statement

All relevant data can be made available on reasonable request to the corresponding author.

References

1. Reissner, E., 1945. The effect of transverse shear deformation on the bending of elastic plates.
2. Mindlin, R.D., 1951. Influence of rotatory inertia and shear on flexural motions of isotropic, elastic plates.
3. Yang, P.C., Norris, C.H. and Stavsky, Y., 1966. Elastic wave propagation in heterogeneous plates. *International Journal of solids and structures*, *2*(4), pp.665-684.
4. Whitney, J.M., 1969. The effect of transverse shear deformation on the bending of laminated plates. *Journal of Composite Materials*, *3*(3), pp.534-547.
5. Whitney, J.M. and Pagano, N.J., 1970. Shear deformation in heterogeneous anisotropic plates.
6. Ambartsumyan, S.A., 1969. Theory of Anisotropic Plates, translated from Russian by T. *Cheron and edited by JE Ashton, Technomic*.
7. Sun, C.T. and Whitney, J.M., 1973. Theories for the dynamic response of laminated plates. *AIAA journal*, *11*(2), pp.178-183.
8. Bert, C.W. and Chen, T.L.C., 1978. Effect of shear deformation on vibration of antisymmetric angle-ply laminated rectangular plates. *International Journal of Solids and Structures*, *14*(6), pp.465-473.
9. Reddy, J.N., 1979. Free vibration of antisymmetric, angle-ply laminated plates including transverse shear deformation by the finite element method. *Journal of Sound and Vibration*, *66*(4), pp.565-576.
10. Noor, A.K. and Burton, W.S., 1989. Stress and free vibration analyses of multilayered composite plates. *Composite Structures*, *11*(3), pp.183-204.
11. Kant, T.A.R.U.N. and Swaminathan, K., 2001. Analytical solutions for free vibration of laminated composite and sandwich plates based on a higher-order refined theory. *Composite structures*, *53*(1), pp.73-85.
12. Thai, H.T. and Kim, S.E., 2010. Free vibration of laminated composite plates using two variable refined plate theory. *International Journal of Mechanical Sciences*, *52*(4), pp.626-633.
13. Thai, H.T. and Choi, D.H., 2013. A simple first-order shear deformation theory for laminated composite plates. *Composite Structures*, *106*, pp.754-763.
14. Vaishali, Mukhopadhyay, T., Karsh, P.K., Basu, B. and Dey, S., 2020. Machine learning based stochastic dynamic analysis of functionally graded shells. *Composite Structures*, *237*, p.111870.
15. Mantari, J.L. and Ore, M., 2015. Free vibration of single and sandwich laminated composite plates by using a simplified FSDT. *Composite Structures*, *132*, pp.952-959.
16. Noor, A.K. and Burton, W.S., 1989. Assessment of shear deformation theories for multilayered composite plates.

17. Reddy, J.N., 1993. An evaluation of equivalent-single-layer and layerwise theories of composite laminates. *Composite structures*, *25*(1-4), pp.21-35.
18. Kant, T., 1993. A critical review and some results of recently developed refined theories of fiber-reinforced laminated composites and sandwiches. *Composite structures*, *23*(4), pp.293-312.
19. Liu, D. and Li, X., 1996. An overall view of laminate theories based on displacement hypothesis. *Journal of composite materials*, *30*(14), pp.1539-1561.
20. Mantari, J.L. and Soares, C.G., 2013. Generalized layerwise HSDT and finite element formulation for symmetric laminated and sandwich composite plates. *Composite Structures*, *105*, pp.319-331.
21. Mantari, J.L., Granados, E.V., Hinostroza, M.A. and Soares, C.G., 2014. Modelling advanced composite plates resting on elastic foundation by using a quasi-3D hybrid type HSDT. *Composite Structures*, *118*, pp.455-471.
22. Reddy, J.N. and Robbins Jr, D.H., 1994. Theories and computational models for composite laminates.
23. Toledano, A. and Murakami, H., 1987. A composite plate theory for arbitrary laminate configurations.
24. Lu, X. and Liu, D., 1992. An interlaminar shear stress continuity theory for both thin and thick composite laminates.
25. Reddy, J.N., 1987. A generalization of two-dimensional theories of laminated composite plates. *Communications in applied numerical methods*, *3*(3), pp.173-180.
26. Tahani, M., 2007. Analysis of laminated composite beams using layerwise displacement theories. *Composite Structures*, *79*(4), pp.535-547.
27. Ramesh, S.S., Wang, C.M., Reddy, J.N. and Ang, K.K., 2009. A higher-order plate element for accurate prediction of interlaminar stresses in laminated composite plates. *Composite Structures*, *91*(3), pp.337-357.
28. Carrera, E., 2003. Theories and finite elements for multilayered plates and shells: a unified compact formulation with numerical assessment and benchmarking. *Archives of Computational Methods in Engineering*, *10*(3), pp.215-296.
29. Chakrabarti, A. and Sheikh, A.H., 2005. Analysis of laminated sandwich plates based on interlaminar shear stress continuous plate theory. *Journal of engineering mechanics*, *131*(4), pp.377-384.
30. Akhras, G. and Li, W., 2007. Spline finite strip analysis of composite plates based on higher-order zigzag composite plate theory. *Composite structures*, *78*(1), pp.112-118.
31. Kulkarni, S.D. and Kapuria, S., 2008. Free vibration analysis of composite and sandwich plates using an improved discrete Kirchhoff quadrilateral element based on third-order zigzag theory. *Computational mechanics*, *42*(6), pp.803-824.
32. Roy, S., Thakur, S.N. and Ray, C., 2021. Free vibration analysis of laminated composite hybrid and GFRP shells based on higher order zigzag theory with experimental validation. *European Journal of Mechanics-A/Solids*, *88*, p.104261.
33. Kumar, A., Chakrabarti, A. and Bhargava, P., 2013. Finite element analysis of laminated composite and sandwich shells using higher order zigzag theory. *Composite Structures*, *106*, pp.270-281.
34. Chakrabarti, A., Chalak, H.D., Iqbal, M.A. and Sheikh, A.H., 2011. A new FE model based on higher order zigzag theory for the analysis of laminated sandwich beam with soft core. *Composite Structures*, *93*(2), pp.271-279.

35. Di Sciuva, M., Gherlone, M., Iurlaro, L. and Tessler, A., 2015. A class of higher-order C0 composite and sandwich beam elements based on the refined zigzag theory. *Composite Structures*, *132*, pp.784-803.
36. Chalak, H.D., Chakrabarti, A., Iqbal, M. and Sheikh, A.H., 2013. Free vibration analysis of laminated soft core sandwich plates. *Journal of Vibration and Acoustics*, *135*(1).
37. Dey, S., Mukhopadhyay, T. and Adhikari, S., 2018. *Uncertainty quantification in laminated composites: a meta-model based approach*. CRC Press.
38. Ke, S., Xu, L. and Ge, Y., 2018. Sensitivity analysis and estimation method of natural frequency for large cooling tower based on field measurement. *Thin-Walled Structures*, *127*, pp.809-821.
39. Rasmussen, C.E. and Nickisch, H., 2010. Gaussian processes for machine learning (GPML) toolbox. *The Journal of Machine Learning Research*, *11*, pp.3011-3015.
40. Vaishali, Mukhopadhyay, T., Kumar, R.R. and Dey, S., 2021. Probing the multi-physical probabilistic dynamics of a novel functional class of hybrid composite shells. *Composite Structures*, *262*, p.113294.
41. Kollar, L.P. and Springer, G.S., 2003. *Mechanics of composite structures*. Cambridge university press.
42. Khandelwal, R.P., Chakrabarti, A. and Bhargava, P., 2015. Vibration response of laminated composite plate having weakly bonded layers. *Applied Mathematical Modelling*, *39*(17), pp.5073-5090.
43. Kulkarni, S.D. and Kapuria, S., 2008. Free vibration analysis of composite and sandwich plates using an improved discrete Kirchhoff quadrilateral element based on third-order zigzag theory. *Computational mechanics*, *42*(6), pp.803-824.
44. Thai, H.T. and Choi, D.H., 2013. A simple first-order shear deformation theory for laminated composite plates. *Composite Structures*, *106*, pp.754-763.
45. Mantari, J.L. and Ore, M., 2015. Free vibration of single and sandwich laminated composite plates by using a simplified FSDT. *Composite Structures*, *132*, pp.952-959.
46. Mukhopadhyay T., 2018. A multivariate adaptive regression splines based damage identification methodology for web core composite bridges including the effect of noise, *Journal of Sandwich Structures & Materials*, 20(7) 885–903
47. Chalak, H. D., Chakrabarti, A., Iqbal, M. A., Sheikh, A. H., 2012. An improved C0 FE model for the analysis of laminated sandwich plate with soft core. *Finite Elements in Analysis and Design*, 56, 20-31.
48. Liu, B., Vu-Bac, N., Zhuang, X., Fu, X. Rabczuk, T., 2022. Stochastic full-range multiscale modeling of thermal conductivity of Polymeric carbon nanotubes composites: A machine learning approach. *Composite Structures*, 289 115393.
49. Mukhopadhyay T., Naskar S., Chakraborty S., Karsh P. K., Choudhury R., Dey S., 2021. Stochastic oblique impact on composite laminates: A concise review and characterization of the essence of hybrid machine learning algorithms, *Archives of Computational Methods in Engineering*, 28 1731–1760
50. Liu, B., Vu-Bac, N. Rabczuk, T., 2021. A stochastic multiscale method for the prediction of the thermal conductivity of Polymer nanocomposites through hybrid machine learning algorithms. *Composite Structures*, 273114269.
51. Dey, S., Mukhopadhyay, T. and Adhikari, S., 2015. Stochastic free vibration analyses of composite shallow doubly curved shells–A Kriging model approach. Composites Part B: Engineering, 70, pp.99-112.

52. Thakur, S.N. and Ray, C., 2015. An accurate C0 finite element model of moderately thick and deep laminated doubly curved shell considering cross sectional warping. Thin-Walled Structures, 94, pp.384-393.
53. Pagani, A. and Carrera, E., 2021. Unified one-dimensional finite element for the analysis of hyperelastic soft materials and structures. Mechanics of Advanced Materials and Structures, pp.1-14.
54. Pagani, A. and Carrera, E., 2018. Unified formulation of geometrically nonlinear refined beam theories. Mechanics of Advanced Materials and Structures, 25(1), pp.15-31.
55. Wu, B., Pagani, A., Filippi, M., Chen, W.Q. and Carrera, E., 2019. Large-deflection and post-buckling analyses of isotropic rectangular plates by Carrera Unified Formulation. International Journal of Non-Linear Mechanics, 116, pp.18-31.
56. Wu, B., Pagani, A., Chen, W.Q. and Carrera, E., 2021. Geometrically nonlinear refined shell theories by Carrera Unified Formulation. Mechanics of Advanced Materials and Structures, 28(16), pp.1721-1741.
57. Carrera, E., Pagani, A., Azzara, R. and Augello, R., 2020. Vibration of metallic and composite shells in geometrical nonlinear equilibrium states. Thin-Walled Structures, 157, p.107131.
58. Pagani, A. and Carrera, E., 2017. Large-deflection and post-buckling analyses of laminated composite beams by Carrera Unified Formulation. Composite Structures, 170, pp.40-52.
59. Garg A., Belarbi M. O., Tounsi A., Li L., Singh A., Mukhopadhyay T., 2022. Predicting elemental stiffness matrix of FG nanoplates using Gaussian Process Regression based surrogate model in framework of layerwise model, Engineering Analysis with Boundary Elements, 143 779-795
60. Isanaka B. R., Mukhopadhyay T., Varma R. K., Kushvaha V., 2022. On exploiting machine learning for failure pattern driven strength enhancement of honeycomb lattice materials, Acta Materialia, 239 118226
61. Mukhopadhyay T., Dey T. K., Dey S., Chakrabarti A., 2015. Optimization of fiber reinforced polymer web core bridge deck – A hybrid approach, Structural Engineering International, 25 (2) 173-183
62. Kushari S., Mukhopadhyay T., Chakraborty A., Dey S., 2022. Probability-based unified sensitivity analysis for multi-objective performances of composite laminates: A surrogate-assisted approach, Composite Structures, 294 115559
63. Sharma A., Mukhopadhyay T., Rangappa S. M., Kushvaha V., 2022. Advances in computational intelligence of polymer composite materials: Machine learning assisted modeling, analysis and design, Archives of Computational Methods in Engineering, 29 3341–3385
64. Mukhopadhyay T., Chakraborty S., Dey S., Adhikari S., Chowdhury R., 2017. A critical assessment of Kriging model variants for high-fidelity uncertainty quantification in dynamics of composite shells, Archives of Computational Methods in Engineering, 24(3) 495–518
65. Petrolo, M., Carrera E., 2021. Selection of element-wise shell kinematics using neural networks. Computers & Structures 244 106425
66. Naskar S., Spatial variability characterisation of laminated composites, PhD thesis, University of Aberdeen, 2018
67. Naskar S., Mukhopadhyay T., Sriramula S., 2019. Spatially varying fuzzy multi-scale uncertainty propagation in unidirectional fibre reinforced composites, Composite Structures, 209 940-967
68. Kumar R. R., Mukhopadhyay T., Naskar S., Pandey K. M., Dey S., 2019. Stochastic low-velocity impact analysis of sandwich plates including the effects of obliqueness and twist, Thin-Walled Structures, 145 106411

69. Karsh P. K., Mukhopadhyay T., Chakraborty S., Naskar S., Dey S. (2019) A hybrid stochastic sensitivity analysis for low-frequency vibration and low-velocity impact of functionally graded plates, Composites Part B: Engineering, 176 107221
70. Naskar S., Mukhopadhyay T., Sriramula S. (2018) Probabilistic micromechanical spatial variability quantification in laminated composites, Composites Part B: Engineering, 151 291-325
71. Bhattacharyya, R., Mahadevan, S., 2022. Calibration and validation of multiscale model for ultimate strength prediction of composite laminates under uncertainty. ASCE-ASME J Risk and Uncert in Engrg Sys Part B Mech Engrg, 8(2) 021205
72. Bhattacharyya, R., Mahadevan, S., & Basu, P. K., 2022). Computationally efficient multiscale modeling for probabilistic analysis of CFRP composites with micro-scale spatial randomness. Composite Structures, 280, 114884